
Uncertainty Quantification via Neural Posterior Principal Components

Elias Nehme

Technion–Israel Institute of Technology
seliasne@campus.technion.ac.il

Omer Yair

Technion–Israel Institute of Technology
omeryair@campus.technion.ac.il

Tomer Michaeli

Technion–Israel Institute of Technology
tomerm@ee.technion.ac.il

Abstract

Uncertainty quantification is crucial for the deployment of image restoration models in safety-critical domains, like autonomous driving and biological imaging. To date, methods for uncertainty visualization have mainly focused on per-pixel estimates. Yet, a heatmap of per-pixel variances is typically of little practical use, as it does not capture the strong correlations between pixels. A more natural measure of uncertainty corresponds to the variances along the principal components (PCs) of the posterior distribution. Theoretically, the PCs can be computed by applying PCA on samples generated from a conditional generative model for the input image. However, this requires generating a very large number of samples at test time, which is painfully slow with the current state-of-the-art (diffusion) models. In this work, we present a method for predicting the PCs of the posterior distribution for any input image, in a single forward pass of a neural network. Our method can either wrap around a pre-trained model that was trained to minimize the mean square error (MSE), or can be trained from scratch to output both a predicted image and the posterior PCs. We showcase our method on multiple inverse problems in imaging, including denoising, inpainting, super-resolution, colorization, and biological image-to-image translation. Our method reliably conveys instance-adaptive uncertainty directions, achieving uncertainty quantification comparable with posterior samplers while being orders of magnitude faster. Code and examples are available on our [webpage](#).

1 Introduction

Reliable uncertainty quantification is central to making informed decisions when using predictive models. This is especially important in domains with high stakes such as autonomous cars and biological/medical imaging, where based on visual data, the system is asked to provide predictions that could influence human life. In such domains, communicating predictive uncertainty becomes a necessity. In the particular case of image-to-image inverse problems, efficient *visualization* of predictive uncertainty is required. For example, in biological and medical image-to-image translation [39, 7, 41, 42], the predicted image as a whole is supposed to inform a scientific discovery or affect the diagnosis of a patient. Hence, an effective form of uncertainty to consider in this case is semantically-coordinated pixel variations that could alter the output image.

Currently, the majority of existing methods handle uncertainty in image-valued inverse problems by factorizing the output posterior into per-pixel marginals, in which case the strong correlations between pixels are completely ignored. This leads to per-pixel uncertainty estimates in the form

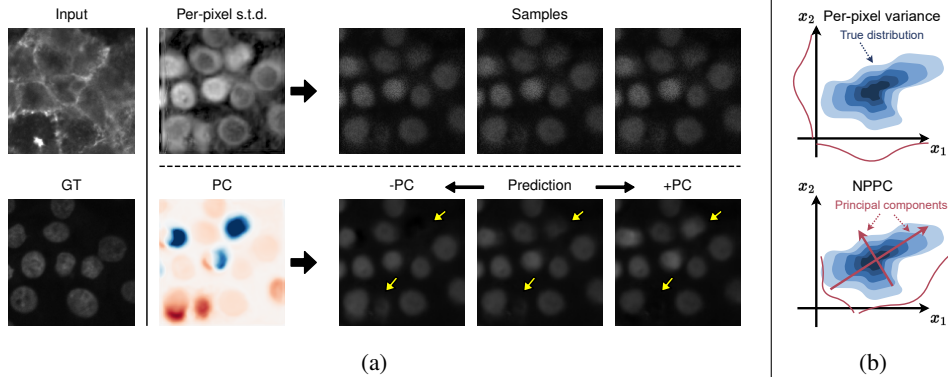


Figure 1: **Comparison between per-pixel methods and NPPC.** In structured output posteriors such as in image-to-image regression (left), uncertainty visualization in the form of per-pixel variance maps (top) fail to convey semantic variations in the prediction, leaving the user with no clue regarding the different possibilities of the solution set. Our method - NPPC (bottom) captures a more natural measure of uncertainty, by providing the user with input-adaptive PCs around the mean prediction. These can then be used to navigate the different possibilities in a meaningful manner. *e.g.*, in 1a NPPC is used to traverse the existence of uncertain cells in an image-to-image translation task from biological imaging. Panel 1b presents a 2D motivating example illustrating the practical benefit of moving along PCs as opposed to the “standard” coordinate system (*e.g.*, pixels in an image).

of variance heatmaps [20] or confidence intervals [2], which are of little practical use as they do not describe the *joint* uncertainty of different pixels. As a result, such models suffer from model misspecification, absorbing inter-pixel covariates into per-pixel marginals, and presenting the user with unnecessarily inflated uncertainty estimates (see Fig. 1b). For example, consider a set of pixels along an edge in an image, in the task of image super-resolution. It is clear that for severe upsampling factors, a model would typically be uncertain around object edges. However, since these pixels are all correlated with the same object, the underlying uncertainty is whether the entire edge is shifted *jointly*, and not whether individual pixels can be shifted independently.

Recently, the field of image-to-image regression has seen a surge of probabilistic methods inspired by advancements in deep generative models, such as diffusion models (DMs). The recurring theme in these approaches is the use of a deep generative prior in order to sample from the posterior distribution [54, 19, 8]. In principle, using the resulting samples, it is possible to present the practitioner with the main modes of variations of the posterior uncertainty, for example using principal components analysis (PCA). However, these powerful posterior samplers come with a heavy computational price. Despite tremendous efforts over the past few years [29, 47, 33, 55], sampling from state-of-the-art methods is still unacceptably slow for many practical applications.

In this work, we bypass the need to learn a data-hungry and extremely slow conditional generative model, by directly training a neural model to predict the principal components of the posterior. Our method, which we term *neural posterior principal components* (NPPC), can wrap around any pre-trained model that was originally trained to minimize the mean square error (MSE), or alternatively can be trained to jointly predict the conditional mean alongside the posterior principal components. In particular, when used as a post-hoc method with MSE pre-trained models, NPPC is a general technique that can be transferred across datasets and model architectures seamlessly. This is because our network architecture inherits the structure and the learning hyper-parameters of the pre-trained model with only one key change: Increasing the filter count at the last layer and employing a Gram-Schmidt process to the output to ensure our found principal components are orthogonal by construction. NPPC is then trained on the pre-trained model residuals, to endow the model’s point prediction with efficient input-adaptive uncertainty visualization.

Several prior works proposed modeling the posterior as a correlated Gaussian distribution. In particular, Dorta et al. [9] approximated the output precision matrix by a matrix of the form $\mathbf{L}\mathbf{L}^T$, where \mathbf{L} is a lower triangular matrix with a pre-determined sparsity pattern. More recently, Monteiro et al. [35] and Meng et al. [32] approximated the covariance matrix by a sum of a diagonal matrix and a low-rank one. However, unlike NPPC, both [9] and [32] are limited to very low-resolution

images, because either they explicitly construct the (huge) covariance matrix during training or they capture only short-range correlations. Moreover, [35] suffers from training instability as multivariate Gaussians with both unknown mean and covariance are known to be notoriously unstable [50]. This limits its applicability to image segmentation, requiring proper background masking to avoid infinite covariance and overflow errors. Our method, on the other hand, does not construct the covariance matrix at any point. It directly outputs the top eigenvectors of the covariance and trains using the objective of PCA. As a result, our method is generally applicable to any inverse problem, enjoys faster and more stable training, and can handle high-resolution images as we demonstrate in Sec. 4. This is enabled by several design choices introduced to the architecture and training, including a Gram-Schmidt output layer, a PCA loss function maximizing correlation with the residuals, and a `Stopgrad` trick that enables learning all principal directions jointly, mitigating the need for training separate models for separate PCs.

We compare our PCs to those extracted from samples from a conditional generative model as recently proposed in [4]. As we show, we obtain comparable results, but orders of magnitude faster. Finally, we showcase NPPC on multiple inverse problems in imaging showing promising results across tasks and datasets. In particular, we apply NPPC to scientific biological datasets, showing the practical benefit of our uncertainty estimates in their ability to capture output correlations.

2 Related Work

Model uncertainty Some methods attempt to report uncertainty that is due to model misspecification and/or out-of-distribution data. Early work on quantification of such uncertainty in deep models has focused on Bayesian modeling by imposing distributions on model weights/feature activations [36, 6, 17]. These methods employ various techniques for approximating the posterior of the weights, including using MCMC [48], variational inference [6, 27], Monte-Carlo Dropout [13], and Laplace approximation [40]. Our work rather focuses on *data* uncertainty as described in Section 3.

Per-pixel methods Some methods for predicting per-pixel variances assume a Gaussian distribution and learn it by maximizing the log-likelihood [20]. This approach was later combined with hierarchical priors on likelihood parameters to infer a family of distributions in a single deterministic neural network [30, 1]. Similarly, multi-modal approximations assuming a Gaussian Mixture Model per pixel have been proposed [5]. Deep Ensembles [23] and Test-time augmentations [57] have also been used to estimate uncertainty by measuring the variance of model predictions. More recently, distribution-free methods such as quantile regression and conformal prediction [43] have taken over their counterparts with firm statistical guarantees. Specifically for image-to-image regression, a work that stands out is that of Angelopoulos et al. [2]. The main shortcoming of these methods is the underlying assumption of *i.i.d.* pixels.

Distribution-free risk control Elaborate distribution-free methods, such as Risk Controlling Prediction Sets (RCPS) [3], take pixel correlations into account by controlling some risk factorizing all pixels in an image (such as the false discovery rate in binary image segmentation). Recently, this approach has been deployed in image-to-image regression problems using a technique called Conformal Prediction Masks [22]. The main drawback of these methods is their inability to explore the different possible options, but rather, only impose upper and lower bounds on the possible solution set. In addition, they also require an extra data split for calibration, which is not always readily available. An interesting recent work in this field [49] has proposed to control the risk of disentangled factors in the latent space of StyleGAN, and demonstrated informative uncertainty visualizations in inverse problems of facial images. However, the main drawbacks of this work are the key assumption of access to disentangled latent representations and the generalization gap from fake to real images.

Generative models and posterior samplers Generative models have been widely used to navigate prediction uncertainty, either in the form of conditional variational autoencoders [51] and conditional GANs [34], or more recently using state-of-the-art score-based and denoising diffusion models [52, 14, 53, 46, 45, 28, 19, 12, 58, 8]. While the latter have achieved astounding results in the last two years, when aiming for high-quality samples, they remain extremely slow to sample from, despite promising results reported in recent efforts [29, 47, 33, 55]. The recent Confusion method [15] finetunes pre-trained diffusion models to output interval bounds in a single forward pass to achieve fast confidence interval prediction for posterior samplers. Nonetheless, the result is a per-pixel uncertainty map.

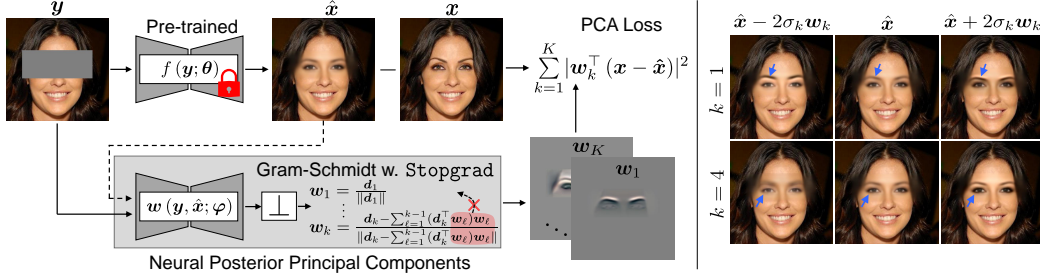


Figure 2: **Method overview.** Here, NPPC is demonstrated for image inpainting, where x is the ground truth image, y is the masked input, and \hat{x} is the posterior mean prediction. Our method can wrap around pre-trained conditional mean predictors $f(y; \theta)$, replicating their architecture with a slight modification at the output (see text). Using a PCA loss on the errors ($e = x - \hat{x}$), we learn to predict the first K PCs of the posterior w_1, \dots, w_K directly in a single forward pass of a neural network $w(y, \hat{x}; \varphi)$. On the right, we visualize the uncertainty captured by two PCs (w_1, w_4) around the mean prediction \hat{x} .

Gaussian covariance approximation Works that are particularly related to the approach presented here are [9], [35] and [32]. Specifically, Dorta et al. [9] proposed to model the output posterior with a correlated Gaussian, and approximated the precision matrix using the factorization $\Lambda = \mathbf{L}\mathbf{L}^\top$, where \mathbf{L} is a lower triangular matrix with predefined sparsity patterns capturing short-term correlations. The matrix \mathbf{L} is then learned during training using a maximum likelihood objective. Similarly, [35] and [32] suggested approximating the posterior covariance matrix using a low-rank factorization with the latter involving second-order scores. However, the main drawback of [9] and [32] is their limited ability to generalize to high-resolution RGB images while efficiently capturing long-range correlations [10]. Additionally, [35] is limited by training instability, limiting its applicability to image segmentation. In contrast, our method directly estimates eigenvectors of the covariance matrix without the need for explicitly storing the covariance matrix in memory during training as in [32]. This enables us to seamlessly generalize to arbitrary inverse problems and high-resolution RGB images with more stable and less expensive training steps.

Concurrent work A related approach was recently proposed in the concurrent work of [31], where the authors demonstrate a training-free method to calculate the posterior PCs in the task of Gaussian denoising. The key advantage of our approach over this work is that we are not constrained to the task of Gaussian denoising and can handle arbitrary inverse problems, as we show in our experiments.

3 Neural Posterior Principal Components

We address the problem of predicting a signal $x \in \mathbb{R}^{d_x}$ based on measurements $y \in \mathbb{R}^{d_y}$. In the context of imaging, y often represents a degraded version of x (e.g., noisy, blurry), or a measurement of the same specimen/scene acquired by a different modality. We assume that x and y are realizations of random vectors \mathbf{x} and \mathbf{y} with an unknown joint distribution $p(\mathbf{x}, \mathbf{y})$, and that we have a training set $\mathcal{D} = \{(\mathbf{x}_i, \mathbf{y}_i)\}_{i=1}^{N_d}$ of matched input-output pairs independently sampled from that distribution.

Many image restoration methods output a single prediction \hat{x} for any given input y . A common choice is to aim for the posterior mean $\hat{x} = \mathbb{E}[\mathbf{x} | \mathbf{y} = \mathbf{y}]$, which is the predictor that minimizes the MSE. However, a single prediction does not convey to the user the uncertainty in the restoration. To achieve this goal, here we propose to also output the top K principal components of the posterior $p(\mathbf{x} | \mathbf{y})$, i.e., the top K eigenvectors of the posterior covariance $\mathbb{E}[(\mathbf{x} - \hat{\mathbf{x}})(\mathbf{x} - \hat{\mathbf{x}})^\top | \mathbf{y} = \mathbf{y}]$. The PCs capture the main directions along which \mathbf{x} could vary, given the input \mathbf{y} , and thus provide the user with valuable information. However, their direct computation is computationally infeasible in high-dimensional settings. The main challenge we face is, therefore, how to obtain the posterior PCs without having to ever store or even compute the entire posterior covariance matrix. Before we describe our method, let us recall the properties of PCA in the standard (unconditional) setting.

Unconditional PCA Given a set of N data points $\{\mathbf{x}_i\}$ where $\mathbf{x}_i \in \mathbb{R}^{d_x}$, the goal in PCA is to find a set of K orthogonal principal directions w_1, \dots, w_K along which the data varies the most. The resulting directions are ordered such that the variance of $\{w_1^\top \mathbf{x}_i\}$ is biggest, the variance of

$\{\mathbf{w}_2^\top \mathbf{x}_i\}$ is the second biggest, etc. The objective function for finding these directions has multiple equivalent forms and interpretations. The one we exploit here is the iterative maximization of variance. Specifically, let \mathbf{X} denote the centered data matrix whose rows consist of different observations \mathbf{x}_i^\top after subtracting their column-wise mean, and let $\mathbf{w}_1, \dots, \mathbf{w}_K$ denote the first K PCs. Then the k^{th} PC is given by

$$\mathbf{w}_k = \arg \max_{\mathbf{w}} \|\mathbf{X}\mathbf{w}\|_2^2, \quad \text{s.t.} \quad \|\mathbf{w}\| = 1, \quad \mathbf{w} \perp \text{span}\{\mathbf{w}_1, \dots, \mathbf{w}_{k-1}\}, \quad (1)$$

where for the first PC, the constraint is only $\|\mathbf{w}\| = 1$. The variance along the k^{th} PC is given by $\sigma_k^2 = \frac{1}{N} \|\mathbf{X}\mathbf{w}_k\|_2^2$.

The challenge in posterior PCA Going back to our goal of computing the posterior PCs, let us assume for simplicity we are given a pre-trained conditional mean predictor $\hat{\mathbf{x}} = f(\mathbf{y}; \boldsymbol{\theta})$ obtained through MSE minimization on the training set \mathcal{D} . Let $e_i = \mathbf{x}_i - \hat{\mathbf{x}}_i$ denote the error of the conditional mean predictor given the i^{th} measurement, $\mathbf{y} = \mathbf{y}_i$. The uncertainty directions we wish to capture per sample \mathbf{y}_i , are the PCs of the error e_i around the conditional mean estimate $\hat{\mathbf{x}}_i$. Conceptually, this task is extremely difficult as during training for every measurement \mathbf{y}_i , we have access only to a *single* error sample e_i . If we were to estimate the PCs directly, the result would be a trivial single principal direction equaling e_i which is unpredictable at test time. To address this challenge, here we propose to harness the implicit bias of neural models and to learn these directions from a dataset of triplets $\mathcal{D}' = \{(\mathbf{x}_i, \mathbf{y}_i, \hat{\mathbf{x}}_i)\}_{i=1}^{N_d}$. The key implicit assumption underlying our approach (and empirical risk minimization in general) is that the posterior mean $\mathbb{E}[\mathbf{x}|\mathbf{y} = \mathbf{y}]$ and the posterior covariance $\mathbb{E}[(\mathbf{x} - \hat{\mathbf{x}})(\mathbf{x} - \hat{\mathbf{x}})^\top | \mathbf{y} = \mathbf{y}]$ vary smoothly with \mathbf{y} . Hence, with the right architecture, such models can capitalize on inter-sample dependencies and properly generalize to unseen test points, by learning posterior PCs that change gracefully as a function of \mathbf{y} . This is much like models trained with MSE minimization to estimate the conditional mean $\mathbb{E}[\mathbf{x}|\mathbf{y} = \mathbf{y}]$, while being presented during training only with a single output \mathbf{x}_i for every measurement \mathbf{y}_i .

3.1 Naive solution: Iterative learning of PCs

Following the intuition from the previous section, we can parameterize the k^{th} PC of the error using a neural network $\mathbf{w}_k(\mathbf{y}, \hat{\mathbf{x}}; \boldsymbol{\varphi}_k)$ with parameters $\boldsymbol{\varphi}_k$, which has similar capacity to the pre-trained model $f(\mathbf{y}; \boldsymbol{\theta})$ outputting the conditional mean. This model accepts the measurement \mathbf{y} and (optionally) the conditional mean estimate $\hat{\mathbf{x}}$, and outputs the k^{th} PC of the error e .

Let $\mathbf{d}_1(\mathbf{y}, \hat{\mathbf{x}}; \boldsymbol{\varphi}_1)$ be a model for predicting the first unnormalized direction, such that $\mathbf{w}_1(\mathbf{y}_i, \hat{\mathbf{x}}_i; \boldsymbol{\varphi}_1) = \mathbf{d}_1(\mathbf{y}_i, \hat{\mathbf{x}}_i; \boldsymbol{\varphi}_1) / \|\mathbf{d}_1(\mathbf{y}_i, \hat{\mathbf{x}}_i; \boldsymbol{\varphi}_1)\|$. Given a dataset of triplets $\mathcal{D}' = \{(\mathbf{x}_i, \mathbf{y}_i, \hat{\mathbf{x}}_i)\}$, we adopt the objective employed in (1), and propose to learn the parameters of the input-dependent first PC by minimizing

$$\mathcal{L}_{\mathbf{w}_1}(\mathcal{D}', \boldsymbol{\varphi}_1) = - \sum_{(\mathbf{x}_i, \mathbf{y}_i, \hat{\mathbf{x}}_i \in \mathcal{D}')} |\mathbf{w}_1(\mathbf{y}_i, \hat{\mathbf{x}}_i; \boldsymbol{\varphi}_1)^\top e_i|^2. \quad (2)$$

Next, given the model predicting the first PC, we can train a model to predict the second PC, $\mathbf{w}_2(\mathbf{y}_i, \hat{\mathbf{x}}_i; \boldsymbol{\varphi}_2)$, by manipulating the output of a model $\mathbf{d}_2(\mathbf{y}_i, \hat{\mathbf{x}}_i; \boldsymbol{\varphi}_2)$. Specifically, following the approach in (1), we optimize the same loss (2), but construct the output of the model \mathbf{w}_2 by removing the projection of \mathbf{d}_2 onto \mathbf{w}_1 , and normalizing the result. This ensures that $\mathbf{w}_2(\mathbf{y}_i, \hat{\mathbf{x}}_i; \boldsymbol{\varphi}_2) \perp \mathbf{w}_1(\mathbf{y}_i, \hat{\mathbf{x}}_i; \boldsymbol{\varphi}_1)$.

While in principle this approach can be iterated K times to learn the first K PCs, it has several drawbacks that make it impractical. First, it requires a prolonged iterative training of K neural networks sequentially, preventing parallelization and leading to very long training times. Second, this approach is also inefficient at test time, as we need to compute K dependent forward passes. Finally, in this current formulation, different PCs have their own set of weights $\{\boldsymbol{\varphi}_k\}_{k=1}^K$, and do not share parameters. This is inefficient as for a given input \mathbf{y} and corresponding mean prediction $\hat{\mathbf{x}}$, it is expected that the initial feature extraction stage for predicting the different PCs, would be similar. A better strategy is therefore to design an architecture that outputs all PCs at once.

3.2 Joint learning of PCs

To jointly learn the first K PCs of the error using a single neural network $\mathbf{w}(\mathbf{y}_i, \hat{\mathbf{x}}_i; \boldsymbol{\varphi})$, we introduce two key changes to the architecture inherited from the pre-trained mean estimator $f(\mathbf{y}; \boldsymbol{\theta})$. First,

the number of filters at the output layer is multiplied by K , to accommodate the K PCs, $\mathbf{w}_1, \dots, \mathbf{w}_K$. Second, we introduce a Gram-Schmidt procedure at the output layer, making the directions satisfy the orthogonality constraint by construction. Formally, denote the non-orthonormal predicted set of directions by $\mathbf{d}_1, \dots, \mathbf{d}_K$. Then, we transform them to be an orthonormal set $\mathbf{w}_1, \dots, \mathbf{w}_K$ as

$$\begin{aligned} \mathbf{w}_1 &= \frac{\mathbf{d}_1}{\|\mathbf{d}_1\|}, \\ \mathbf{w}_k &= \frac{\mathbf{d}_k - \sum_{\ell=1}^{k-1} (\mathbf{d}_k^\top \mathbf{w}_\ell) \mathbf{w}_\ell}{\|\mathbf{d}_k - \sum_{\ell=1}^{k-1} (\mathbf{d}_k^\top \mathbf{w}_\ell) \mathbf{w}_\ell\|}, \quad k = 2, \dots, K. \end{aligned} \quad (3)$$

Note, however, that these changes do not yet guarantee proper learning of the PCs. Indeed, if we were to learn the directions by naively minimizing the loss

$$\mathcal{L}_{\mathbf{w}}(\mathcal{D}', \varphi) = - \sum_{(\mathbf{x}_i, \mathbf{y}_i, \hat{\mathbf{x}}_i \in \mathcal{D}')} \sum_{k=1}^K |\mathbf{w}_k(\mathbf{y}_i, \hat{\mathbf{x}}_i; \varphi)^\top \mathbf{e}_i|^2, \quad (4)$$

then we would only recover them up to an orthogonal matrix. To see this, let \mathbf{W}_i denote the matrix that has $\mathbf{w}_k(\mathbf{y}_i, \hat{\mathbf{x}}_i; \varphi)$ in its k^{th} column. Then the inner sum in (4) can be rewritten as $\|\mathbf{W}_i^\top \mathbf{e}_i\|_2^2$. Now, it is easy to see that neither the loss nor the constraints are affected by replacing each \mathbf{W}_i with $\tilde{\mathbf{W}}_i = \mathbf{W}_i \mathbf{O}_i$, for some orthogonal matrix \mathbf{O}_i . Indeed, this solution satisfies the orthogonality constraint $\tilde{\mathbf{W}}_i^\top \tilde{\mathbf{W}}_i = \mathbf{I}$, and attains the same loss value as the original PCs.

Note that this rotation ambiguity did not exist in the naive approach of Sec. 3.1 because there, when finding the k^{th} PC given the preceding $k-1$ pre-trained PCs, the loss term $|\mathbf{w}_k(\mathbf{y}_i, \hat{\mathbf{x}}_i; \varphi)^\top \mathbf{e}_i|^2$ did not affect the learning of $\mathbf{w}_1, \dots, \mathbf{w}_{k-1}$. However, when attempting to learn all directions jointly, the preceding PCs receive a gradient signal from the k^{th} loss term as \mathbf{w}_k is a function of $\mathbf{w}_1, \dots, \mathbf{w}_{k-1}$ in the Gram-Schmidt procedure.

To solve this problem and decouple the learning of the different PCs while still maintaining their orthogonality, we propose a simple modification to the Gram-Schmidt procedure: Using Stopgrad for the previously derived PCs within the projection operators in (3) (see the **red term** in Fig. 2). This way, in each learning step the different PCs are guaranteed to be orthogonal, while solely optimizing their respective objective. This allows learning them jointly and recovering the solution of the iterative scheme in a single forward pass of a neural network with shared parameters. Please see App. D.2 for validation of the equivalence between sequential and joint PC learning.

3.3 Learning variances along PCs

Recall that the variance along the k^{th} direction corresponds to the average squared projection of the data along that direction. We can use that to output a prediction of the variances $\{\sigma_k^2\}$ of the PCs, by using a loss that minimizes $\sum_i (\sigma_k^2 - |\mathbf{w}_k^\top \mathbf{e}_i|^2)^2$ for every k . However, instead of adding K additional outputs to the architecture, we can encode the variances in the norms of the unnormalized directions. To achieve this without altering the optimization objective for finding the k^{th} PC, we again invoke the Stopgrad operator on the term $|\mathbf{w}_k^\top \mathbf{e}_i|^2$ which is the current loss function value, and match the norm of the found PCs at the current step to this projected variance by minimizing the loss

$$\mathcal{L}_\sigma(\mathcal{D}', \varphi) = \sum_{(\mathbf{x}_i, \mathbf{y}_i, \hat{\mathbf{x}}_i \in \mathcal{D}')} \sum_{k=1}^K \left(\left\| \mathbf{d}_k - \sum_{\ell=1}^{k-1} (\mathbf{d}_k^\top \mathbf{w}_\ell) \mathbf{w}_\ell \right\|_2^2 - |\mathbf{w}_k^\top \mathbf{e}_i|^2 \right)^2. \quad (5)$$

With this, our prediction for σ_k^2 at test-time is simply $\|\mathbf{d}_k - \sum_{\ell=1}^{k-1} (\mathbf{d}_k^\top \mathbf{w}_\ell) \mathbf{w}_\ell\|_2^2$. Please see App. D.3 for quantitative validation of our estimated variances.

3.4 Joint prediction of posterior mean

Thus far, we assumed we have access to a pre-trained posterior mean predictor $\hat{\mathbf{x}} = f(\mathbf{y}; \boldsymbol{\theta})$, obtained through MSE minimization on a dataset $\mathcal{D} = \{(\mathbf{x}_i, \mathbf{y}_i)\}_{i=1}^{N_d}$ of matched pairs. Hence, our entire derivation revolved around a dataset of triplets $\mathcal{D}' = \{(\mathbf{x}_i, \mathbf{y}_i, \hat{\mathbf{x}}_i)\}_{i=1}^{N_d}$. However, this is not strictly necessary. In particular, the posterior mean predictor can be learned jointly alongside the PCs with an

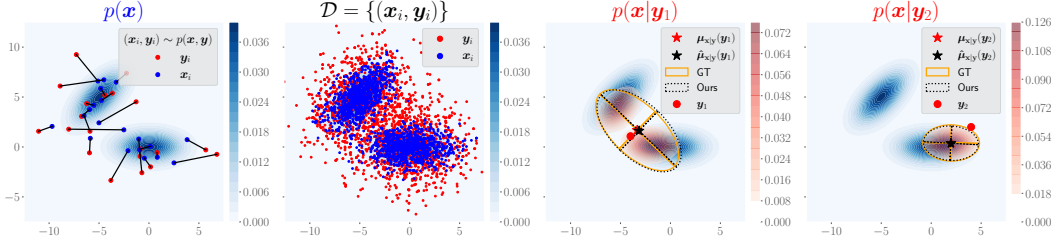


Figure 3: **Denoising samples from a 2D Gaussian mixture.** The left two panels depict the underlying (unknown) signal prior $p(\mathbf{x})$ (blue heatmap), exemplar matched samples from the joint distribution $(\mathbf{x}_i, \mathbf{y}_i) \sim p(\mathbf{x}, \mathbf{y})$, and the resulting training set \mathcal{D} . The right two panels show the analytical posterior $p(\mathbf{x}|\mathbf{y})$ (red heatmap) for two different test points \mathbf{y}_1 and \mathbf{y}_2 (marked as red dots) on top of the signal prior. Our estimated conditional mean $\hat{\boldsymbol{\mu}}_{\mathbf{x}|\mathbf{y}}(\mathbf{y})$ (black star) and PCs scaled by the estimated std (dashed black ellipse) coincide with the analytical posterior mean $\boldsymbol{\mu}_{\mathbf{x}|\mathbf{y}}(\mathbf{y})$ (red star), and scaled posterior PCs derived from the analytical covariance (solid orange ellipse).

additional MSE loss

$$\mathcal{L}_{\boldsymbol{\mu}}(\mathcal{D}, \varphi) = \sum_{(\mathbf{x}_i, \mathbf{y}_i) \in \mathcal{D}} \|\mathbf{x}_i - \hat{\mathbf{x}}_i\|_2^2. \quad (6)$$

Note that we do not want the gradients of \mathcal{L}_w and \mathcal{L}_σ to affect the recovered mean. Therefore, we use a Stopgrad operator when inputting the error $\mathbf{x}_i - \hat{\mathbf{x}}_i$ to those loss functions.

3.5 Putting it all together

To summarize, given a dataset $\mathcal{D} = \{(\mathbf{x}_i, \mathbf{y}_i)\}_{i=1}^{N_d}$ of matched pairs, we can learn a model that predicts the posterior mean as well as the posterior PCs, using the combined loss functions of eqs. (4)-(6),

$$\mathcal{L}_{\text{all}} = \mathcal{L}_{\boldsymbol{\mu}} + \lambda_1 \mathcal{L}_w + \lambda_2 \mathcal{L}_\sigma, \quad (7)$$

where λ_1 and λ_2 are weights balancing the contributions of the different losses.

4 Experiments

We now illustrate NPPC on several tasks and datasets. In all experiments except for the toy example, we used variants of the U-Net architecture [44, 11]. The weighting factors for the losses were chosen such that all three terms are roughly within an order of magnitude of each other. Empirically, we find that ramping up the weight factors for the terms of the directions and the variances after the mean estimate started converging, stabilizes training. Full details regarding the architectures, the scheduler, and the per-task setting of λ_1, λ_2 are in App. A.

Toy examples Figure 3 demonstrates NPPC on a 2D denoising task, where samples \mathbf{x}_i from a two-component Gaussian mixture model are contaminated by additive white Gaussian noise to result in noisy measurements \mathbf{y}_i . To predict \mathbf{x} from \mathbf{y} , we trained a 5-layer MLP with 256 hidden features using MSE minimization, and around the estimated conditional mean $\hat{\mathbf{x}} = \hat{\boldsymbol{\mu}}_{\mathbf{x}|\mathbf{y}}(\mathbf{y})$, we trained NPPC (instantiated with a similar MLP) to output the two PCs

$\mathbf{w}_1, \mathbf{w}_2$, and their variances $\hat{\sigma}_1^2, \hat{\sigma}_2^2$. As can be seen in the right two panels of Fig. 3, NPPC accurately predicts the ground-truth (GT) PCs (those are computed from the analytical expression for the posterior covariance; see App. B). To quantify the accuracy of the recovered PCs, we computed the Wasserstein 2-distance between a Gaussian approximation of the GT posterior $p(\mathbf{x}|\mathbf{y}) \approx \mathcal{N}(\boldsymbol{\mu}_{\mathbf{x}|\mathbf{y}}, \boldsymbol{\Sigma}_{\mathbf{x}|\mathbf{y}})$, and an estimated Gaussian constructed by NPPC, $\hat{p}(\mathbf{x}|\mathbf{y}) = \mathcal{N}(\hat{\boldsymbol{\mu}}_{\mathbf{x}|\mathbf{y}}, \mathbf{W}_* \mathbf{W}_*^\top)$, where \mathbf{W}_* has the scaled estimated PC $\hat{\sigma}_k \mathbf{w}_k$ in its k th column. Compared to a baseline of a point mass at the estimated

Table 1: Comparison of the Wasserstein 2-distance from the rank K Gaussian approximation of the GT posterior $p(\mathbf{x}|\mathbf{y}) \approx \mathcal{N}(\boldsymbol{\mu}_{\mathbf{x}|\mathbf{y}}, \boldsymbol{\Sigma}_{\mathbf{x}|\mathbf{y}})$ (i.e., $K = \text{rank}(\boldsymbol{\Sigma}_{\mathbf{x}|\mathbf{y}})$), on 5000 test samples (see text).

	$K=0$	$K=3$	$K=6$	$K=9$	$K=12$
Baseline	0.4	180.6	272.5	317.5	325.7
NPPC	0.4	30.3	31.2	26.6	28.8

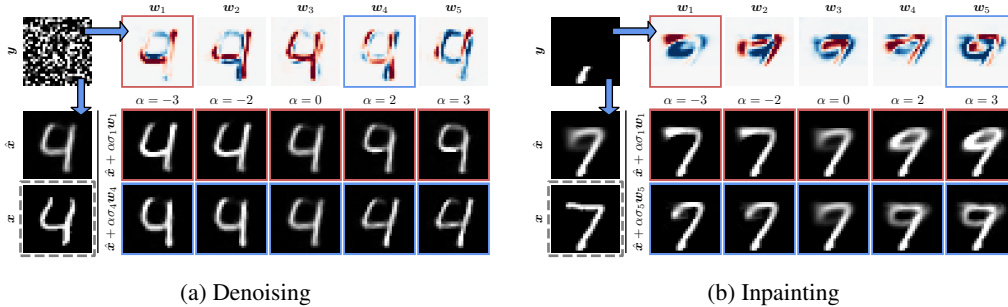


Figure 4: **MNIST denoising and inpainting.** (a) Here we show the application of NPPC to extreme image denoising. On the left is the noisy measurement y , the estimated conditional mean \hat{x} , and the (unknown) ground truth test image x . On the right, the top row shows the first $K = 5$ predicted PCs w_k , and the bottom rows show a traversal of 3 standard deviations around \hat{x} for w_1, w_4 . At an extreme noise level of $\sigma_\varepsilon = 1$, the digit is either a “4” or a “9”. (b) Here we show the result of NPPC on image inpainting from only the 8 bottom rows. The PCs reveal the digit is either a “7” or a “9”.

conditional mean, $\delta(x - \hat{x})$, NPPC reduces the Wasserstein 2-distance by $100\times$ from 4.05 to 0.04. Similarly, we also applied NPPC to a 100-dimensional Gaussian mixture denoising task, and computed the Wasserstein 2-distance from a Gaussian distribution whose mean is the GT posterior mean and whose covariance is the best rank- K approximation of the GT posterior covariance. As clearly evident in Table 1, NPPC maintains a roughly constant distance to the analytical posterior, while the point mass baseline distance rapidly grows with K . See App. B for more details.

Handwritten digits Figure 4 demonstrates NPPC on denoising and inpainting of handwritten digits from the MNIST dataset. In the denoising task, we used noise of standard deviation $\sigma_\varepsilon = 1$, and in inpainting we used a mask that covers the top 70% of the image. As can be seen, for denoising, the learned PCs capture both inter-digit and intra-digit variations, *e.g.*, turning a “4” into a “9”. Similarly, in inpainting, the learned PCs traverse the two likely modes around the mean estimate \hat{x} , going from a “7” into a “9”. More examples are available in App. D.

Faces To test NPPC on faces, we trained on the CelebA-HQ dataset using the original split inherited from celebA [26], resulting in 24183 images for training, 2993 images for validation, and 2824 images for testing. Figure 5 presents results on 256×256 face images from the CelebA-HQ dataset. Here, we demonstrate NPPC on the task of inpainting, as well as on noisy $8\times$ super-resolution with a box downsampling filter and a noise-level of $\sigma_\varepsilon = 0.05$. As can be seen, the PCs generated by NPPC capture semantically meaningful uncertainty, corresponding to the eyes, mouth, and eyebrows. We also tested our approach on inpainting of the eyes area, on $4\times$ super-resolution (noisy and noiseless), and on image colorization. More results and examples are provided in App. D.

Comparison to posterior samplers While traversal along the predicted PCs is valuable for qualitative analysis, an important question is how our single forward pass PCs fair against state-of-the-art posterior samplers. To test this, we now compare NPPC to recent posterior samplers on CelebA-HQ 256×256 . Specifically, we compare NPPC to DDRM [19], DDNM [58], RePaint [28], and MAT [25] on the tasks of image super-resolution/inpainting. We use each of these methods to generate 100 samples per test image, and compute PCA on those samples. We perform comparisons over 100 test images randomly sampled from the FFHQ dataset [18]. Note that NPPC and MAT were trained on the training images of CelebA-HQ according to the original split of CelebA, whereas DDRM, DDNM, and RePaint rely on DDPM [14] as a generative prior, which was trained on the entirety of CelebA-HQ. The results are reported in Table 2. As can be seen, NPPC achieves similar root MSE (RMSE) $\|x - \hat{x}\|_2$, and residual error magnitude $\|e - \mathbf{W}\mathbf{W}^\top e\|_2$ using the first $K = 5$ PCs. This is while being $100\times$ faster than MAT, and $10^3 - 10^5\times$ faster than diffusion-based methods. It is interesting to note that the principal angle between the subspace computed by NPPC and that computed by the baselines, is typically $\approx 90^\circ$. Namely, they are nearly orthogonal. This can be attributed to the severe ill-posedness of the tested settings, resulting in multiple different PCs with roughly the same projected variance. This is also evident in the residual error magnitude, suggesting that a very large number of PCs is required to handle such extreme degradations (see App. C).

Biological image-to-image translation image-to-image translation refers to translating images from one domain into another [16]. In biological imaging, image-to-image translation has been

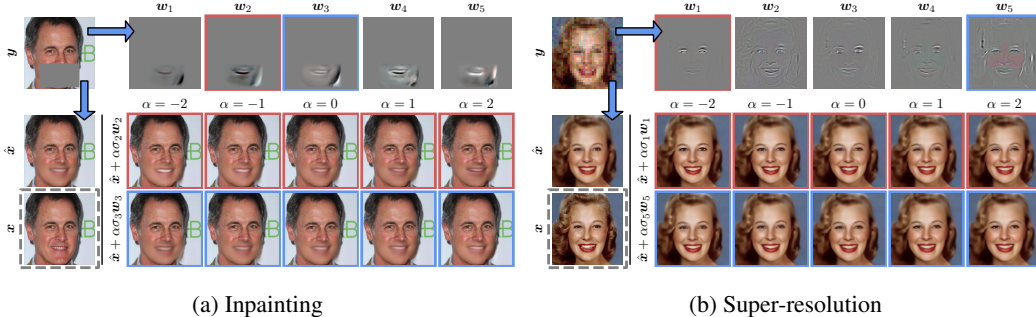


Figure 5: **CelebA-HQ inpainting and $8\times$ noisy super-resolution.** (a) Application of NPPC to image inpainting with a mask around the mouth. NPPC received the masked image y and the mean prediction \hat{x} , and predicted the first 5 posterior PCs w_1, \dots, w_5 . On the bottom, we show a traversal of 2 standard deviations around the mean estimate \hat{x} for w_2 and w_3 , capturing uncertainty regarding open/closed mouth, and background vs shadow next to the jawline. (b) Application of NPPC to $8\times$ noisy super-resolution with a noise standard deviation $\sigma_\varepsilon = 0.05$. Similarly, the PC traversals on the bottom capture uncertainty of eye size and cheek color/position.

Table 2: Quantitative comparison of $\|x - \hat{x}\|_2 \downarrow / \|e - WW^\top e\|_2 \downarrow$ with posterior samplers on 100 test images from FFHQ. Mean prediction and PCs were computed using 100 samples per test image, and compute is reported in neural function evaluations (NFEs).

	Super-resolution				Inpainting		NFEs \downarrow
	4 \times noiseless	4 \times noisy	8 \times noiseless	8 \times noisy	Eyes	Mouth	
DDRM [19]	8.94/8.89	11.29/11.25	13.68/13.47	16.20/16.00	-/-	-/-	$2 \cdot 10^3$
DDNM [58]	8.43/8.38	10.74/10.70	13.12/12.95	15.73/15.55	13.27/11.24	13.30/10.37	$10 \cdot 10^3$
RePaint [28]	-/-	-/-	-/-	-/-	12.24/10.3	12.55/9.72	$457 \cdot 10^3$
MAT [25]	-/-	-/-	-/-	-/-	14.12/12.94	13.08/11.74	100
NPPC (Ours)	8.4/8.24	10.41/10.35	13.06/12.87	15.29/15.11	13.55/11.43	12.23/10.27	1

applied in several contexts, including for predicting fluorescent labels from bright-field images [39] and for predicting one fluorescent label (*e.g.*, nuclear stainings) from another (*e.g.*, actin stainings) [56]. However, unlike its use for artistic purposes, the use of image-to-image translation in biological imaging requires caution. Specifically, without proper uncertainty quantification, predicting cell nuclei from other fluorescent labels could lead to biased conclusions, as cell counting and tracking play central roles in microscopy-based scientific experiments (*e.g.*, drug testing). Here, we applied NPPC to a dataset of migrating cells imaged live for 14h (1 picture every 10min) using a spinning-disk microscope [56]. The dataset consisted of 1753 image pairs of resolution 1024×1024 , out of which 1748 were used for training, and 5 were used for testing following the original split by the authors. We started by training a standard U-Net [44, 11] model using MSE minimization to predict nuclear stainings from actin stainings (see Fig. 6), and then trained NPPC on the residuals. As we show in Fig. 6, the PCs learned by NPPC convey important information to experimenters. For example, the first PC highlights the fact that accurate intensity estimation is not possible in this task, and thereby a global bias is a valid uncertainty component. Furthermore, the remaining PCs reflect semantic uncertainty by adding/removing cells from the conditional mean estimate \hat{x} , thereby clearly communicating reconstruction ambiguity to the user.

5 Discussion

We proposed an approach for directly predicting posterior PCs and showed its applicability across multiple tasks and datasets. Nonetheless, our method does not come without limitations. First, as evident by both the PCs of NPPC and of posterior samplers, for severely ill-posed inverse problems a linear subspace with a small number of PCs captures very little of the error. Hence, a large number of PCs is required to faithfully reconstruct the error. However, the main premise of this work was scientific imaging where scientists usually take reliable measurements, and the uncertainty is not as severe as ultimately the result should drive scientific discovery. Second, throughout this paper, we

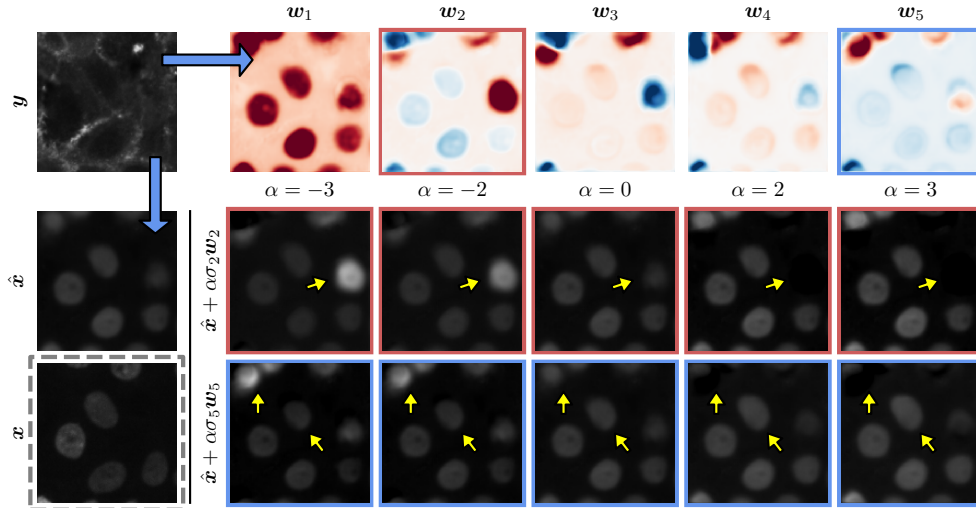


Figure 6: **Biological image-to-image translation.** NPPC applied to the task of translating one fluorescent label y (actin staining) to another fluorescent label x (nuclear staining) in migrating cells (left). On the right, we show the predicted PCs at the top, and traversals along the rows. Yellow arrows point to captured uncertain cells in \hat{x} (either deforming or being completely erased).

learned the PCs on the same training set of the conditional mean estimator. However, generalization error between training and validation could lead to biased PCs estimation as the learning process is usually stopped after some amount of overfitting (*e.g.*, until the validation loss stagnates). This can be solved by using an additional data split for “calibration” as is typically the case with distribution-free methods [43, 3, 2, 49]. Third, different inputs y_i may have posteriors of different complexities, and may thus require a different number of PCs K . In our approach, K is hard-coded within the network’s architecture (it is the number of network outputs). Namely, we treat K as a hyper-parameter that needs to be set in advance prior to training, acting as an upper bound on the number of directions the user may be interested in exploring at test time. However, recall that NPPC also predicts the standard deviations along each of the K PCs. These may serve to decide whether to ignore some of the PCs. Fourth, our learned PCs cover the entire image, whereas in some cases the interesting uncertainty structure could be local (*e.g.*, cell data). In such circumstances, NPPC should either be applied patch-wise or the number of PCs K should be sufficiently increased. Finally, our method is tailored towards capturing uncertainty and not sampling from the posterior. While we provide the directed standard deviations, shifting along a certain direction does not guarantee samples along the way to be on the image data manifold. This can be tackled by employing NPPC in the latent space of a powerful encoder, in which case small enough steps could lead to changes on the manifold in the output image. However, this is beyond the scope of this current work.

6 Conclusion

To conclude, in this work we proposed a technique for directly estimating the principal components of the posterior distribution using a single forward pass in a neural network. We discussed key design choices, including a Gram-Schmidt procedure with a Stopgrad operator, and a principled PCA loss function. Through extensive experiments, we validated NPPC across tasks and domains, showing its wide applicability. We showed that NPPC achieves comparable uncertainty quantification to the naive approach of applying PCA on samples generated by posterior samplers while being orders of magnitude faster. Finally, we applied NPPC to the challenging task of biological image-to-image translation, demonstrating its practical benefit for safety-critical applications. In terms of broader impact, proper uncertainty quantification is crucial for trustworthy interpretable systems, particularly in healthcare applications. Thus, a method for reporting and conveniently visualizing prediction uncertainty could support users and help them avoid making flawed decisions.

Acknowledgements

This research was partially supported by the Israel Science Foundation (grant no. 2318/22), by the Ollendorff Minerva Center, ECE faculty, Technion, and by a gift from KLA. The authors gratefully acknowledge fruitful discussions with Daniel Freedman, Regev Cohen, and Rotem Mulayoff throughout this work. The authors also thank Matan Kleiner, Hila Manor, and Noa Cohen for their help with the figures.

References

- [1] Alexander Amini, Wilko Schwarting, Ava Soleimany, and Daniela Rus. Deep evidential regression. *Advances in Neural Information Processing Systems*, 33:14927–14937, 2020.
- [2] Anastasios N Angelopoulos, Amit P Kohli, Stephen Bates, Michael I Jordan, Jitendra Malik, Thayer Alshaabi, Srigoikul Upadhyayula, and Yaniv Romano. Image-to-image regression with distribution-free uncertainty quantification and applications in imaging. In *International Conference on Machine Learning*, 2022.
- [3] Stephen Bates, Anastasios Angelopoulos, Lihua Lei, Jitendra Malik, and Michael Jordan. Distribution-free, risk-controlling prediction sets. *Journal of the ACM (JACM)*, 68(6):1–34, 2021.
- [4] Omer Belhasin, Yaniv Romano, Daniel Freedman, Ehud Rivlin, and Michael Elad. Principal uncertainty quantification with spatial correlation for image restoration problems. *arXiv preprint arXiv:2305.10124*, 2023.
- [5] Christopher M Bishop. Mixture density networks. 1994.
- [6] Charles Blundell, Julien Cornebise, Koray Kavukcuoglu, and Daan Wierstra. Weight uncertainty in neural network. In *International conference on machine learning*, pages 1613–1622. PMLR, 2015.
- [7] Eric M Christiansen, Samuel J Yang, D Michael Ando, Ashkan Javaherian, Gaia Skibinski, Scott Lipnick, Elliot Mount, Alison O’neil, Kevan Shah, Alicia K Lee, et al. In silico labeling: predicting fluorescent labels in unlabeled images. *Cell*, 173(3):792–803, 2018.
- [8] Hyungjin Chung, Jeongsol Kim, Michael Thompson Mccann, Marc Louis Klasky, and Jong Chul Ye. Diffusion posterior sampling for general noisy inverse problems. In *The Eleventh International Conference on Learning Representations*, 2022.
- [9] Garoe Dorta, Sara Vicente, Lourdes Agapito, Neill DF Campbell, and Ivor Simpson. Structured uncertainty prediction networks. In *Proceedings of the IEEE conference on computer vision and pattern recognition*, pages 5477–5485, 2018.
- [10] Garoe Dorta, Sara Vicente, Lourdes Agapito, Neill DF Campbell, and Ivor Simpson. Training vaes under structured residuals. *arXiv preprint arXiv:1804.01050*, 2018.
- [11] Thorsten Falk, Dominic Mai, Robert Bensch, Özgün Çiçek, Ahmed Abdulkadir, Yassine Marrakchi, Anton Böhm, Jan Deubner, Zoe Jäckel, Katharina Seiwald, et al. U-net: deep learning for cell counting, detection, and morphometry. *Nature methods*, 16(1):67–70, 2019.
- [12] Berthy T Feng, Jamie Smith, Michael Rubinstein, Huiwen Chang, Katherine L Bouman, and William T Freeman. Score-based diffusion models as principled priors for inverse imaging. *arXiv preprint arXiv:2304.11751*, 2023.
- [13] Yarin Gal and Zoubin Ghahramani. Dropout as a bayesian approximation: Representing model uncertainty in deep learning. In *international conference on machine learning*, pages 1050–1059. PMLR, 2016.
- [14] Jonathan Ho, Ajay Jain, and Pieter Abbeel. Denoising diffusion probabilistic models. *Advances in Neural Information Processing Systems*, 33:6840–6851, 2020.

- [15] Eliahu Horwitz and Yedid Hoshen. Confusion: Confidence intervals for diffusion models. *arXiv preprint arXiv:2211.09795*, 2022.
- [16] Phillip Isola, Jun-Yan Zhu, Tinghui Zhou, and Alexei A Efros. Image-to-image translation with conditional adversarial networks. In *Proceedings of the IEEE conference on computer vision and pattern recognition*, pages 1125–1134, 2017.
- [17] Pavel Izmailov, Wesley J Maddox, Polina Kirichenko, Timur Garipov, Dmitry Vetrov, and Andrew Gordon Wilson. Subspace inference for bayesian deep learning. In *Uncertainty in Artificial Intelligence*, pages 1169–1179. PMLR, 2020.
- [18] Tero Karras, Samuli Laine, and Timo Aila. A style-based generator architecture for generative adversarial networks. In *Proceedings of the IEEE/CVF conference on computer vision and pattern recognition*, pages 4401–4410, 2019. URL <https://github.com/NVLabs/ffhq-dataset>.
- [19] Bahjat Kawar, Michael Elad, Stefano Ermon, and Jiaming Song. Denoising diffusion restoration models. In *Advances in Neural Information Processing Systems*, 2022.
- [20] Alex Kendall and Yarin Gal. What uncertainties do we need in bayesian deep learning for computer vision? *Advances in neural information processing systems*, 30, 2017.
- [21] Diederik P Kingma and Jimmy Ba. Adam: A method for stochastic optimization. *International Conference on Learning Representations*, 3, 2015.
- [22] Gilad Kutieli, Regev Cohen, Michael Elad, Daniel Freedman, and Ehud Rivlin. Conformal prediction masks: Visualizing uncertainty in medical imaging. In *ICLR 2023 Workshop on Trustworthy Machine Learning for Healthcare*.
- [23] Balaji Lakshminarayanan, Alexander Pritzel, and Charles Blundell. Simple and scalable predictive uncertainty estimation using deep ensembles. *Advances in neural information processing systems*, 30, 2017.
- [24] Gustav Larsson, Michael Maire, and Gregory Shakhnarovich. Learning representations for automatic colorization. In *Computer Vision—ECCV 2016: 14th European Conference, Amsterdam, The Netherlands, October 11–14, 2016, Proceedings, Part IV 14*, pages 577–593. Springer, 2016.
- [25] Wenbo Li, Zhe Lin, Kun Zhou, Lu Qi, Yi Wang, and Jiaya Jia. Mat: Mask-aware transformer for large hole image inpainting. In *Proceedings of the IEEE/CVF conference on computer vision and pattern recognition*, pages 10758–10768, 2022.
- [26] Ziwei Liu, Ping Luo, Xiaogang Wang, and Xiaoou Tang. Deep learning face attributes in the wild. In *Proceedings of the IEEE International Conference on Computer Vision*, pages 3730–3738, 2015. URL <http://mmlab.ie.cuhk.edu.hk/projects/CelebA.html>.
- [27] Christos Louizos and Max Welling. Multiplicative normalizing flows for variational bayesian neural networks. In *International Conference on Machine Learning*, pages 2218–2227. PMLR, 2017.
- [28] Andreas Lugmayr, Martin Danelljan, Andres Romero, Fisher Yu, Radu Timofte, and Luc Van Gool. Repaint: Inpainting using denoising diffusion probabilistic models. In *Proceedings of the IEEE/CVF Conference on Computer Vision and Pattern Recognition*, pages 11461–11471, 2022.
- [29] Eric Luhman and Troy Luhman. Knowledge distillation in iterative generative models for improved sampling speed. *arXiv preprint arXiv:2101.02388*, 2021.
- [30] Andrey Malinin and Mark Gales. Predictive uncertainty estimation via prior networks. *Advances in neural information processing systems*, 31, 2018.
- [31] Hila Manor and Tomer Michaeli. On the posterior distribution in denoising: Application to uncertainty quantification. *arXiv preprint arXiv:2309.13598*, 2023.

- [32] Chenlin Meng, Yang Song, Wenzhe Li, and Stefano Ermon. Estimating high order gradients of the data distribution by denoising. *Advances in Neural Information Processing Systems*, 34: 25359–25369, 2021.
- [33] Chenlin Meng, Ruiqi Gao, Diederik P Kingma, Stefano Ermon, Jonathan Ho, and Tim Salimans. On distillation of guided diffusion models. In *NeurIPS 2022 Workshop on Score-Based Methods*, 2022.
- [34] Mehdi Mirza and Simon Osindero. Conditional generative adversarial nets. *arXiv preprint arXiv:1411.1784*, 2014.
- [35] Miguel Monteiro, Loïc Le Folgoc, Daniel Coelho de Castro, Nick Pawlowski, Bernardo Marques, Konstantinos Kamnitsas, Mark van der Wilk, and Ben Glocker. Stochastic segmentation networks: Modelling spatially correlated aleatoric uncertainty. *Advances in neural information processing systems*, 33:12756–12767, 2020.
- [36] Radford M Neal. *Bayesian learning for neural networks*, volume 118. Springer Science & Business Media, 2012.
- [37] Alexander Quinn Nichol and Prafulla Dhariwal. Improved denoising diffusion probabilistic models. In *International Conference on Machine Learning*, pages 8162–8171. PMLR, 2021.
- [38] Augustus Odena, Vincent Dumoulin, and Chris Olah. Deconvolution and checkerboard artifacts. *Distill*, 2016. doi: 10.23915/distill.00003. URL <http://distill.pub/2016/deconv-checkerboard>.
- [39] Chawin Ounkomol, Sharmishta Seshamani, Mary M Maleckar, Forrest Collman, and Gregory R Johnson. Label-free prediction of three-dimensional fluorescence images from transmitted-light microscopy. *Nature methods*, 15(11):917–920, 2018.
- [40] Hippolyt Ritter, Aleksandar Botev, and David Barber. A scalable laplace approximation for neural networks. In *6th International Conference on Learning Representations, ICLR 2018- Conference Track Proceedings*, volume 6. International Conference on Representation Learning, 2018.
- [41] Yair Rivenson, Tairan Liu, Zhensong Wei, Yibo Zhang, Kevin de Haan, and Aydogan Ozcan. Phasestain: the digital staining of label-free quantitative phase microscopy images using deep learning. *Light: Science & Applications*, 8(1):23, 2019.
- [42] Yair Rivenson, Hongda Wang, Zhensong Wei, Kevin de Haan, Yibo Zhang, Yichen Wu, Harun Günaydin, Jonathan E Zuckerman, Thomas Chong, Anthony E Sisk, et al. Virtual histological staining of unlabelled tissue-autofluorescence images via deep learning. *Nature biomedical engineering*, 3(6):466–477, 2019.
- [43] Yaniv Romano, Evan Patterson, and Emmanuel Candes. Conformalized quantile regression. *Advances in neural information processing systems*, 32, 2019.
- [44] Olaf Ronneberger, Philipp Fischer, and Thomas Brox. U-net: Convolutional networks for biomedical image segmentation. In *Medical Image Computing and Computer-Assisted Intervention–MICCAI 2015: 18th International Conference, Munich, Germany, October 5-9, 2015, Proceedings, Part III 18*, pages 234–241. Springer, 2015.
- [45] Chitwan Saharia, William Chan, Huiwen Chang, Chris Lee, Jonathan Ho, Tim Salimans, David Fleet, and Mohammad Norouzi. Palette: Image-to-image diffusion models. In *ACM SIGGRAPH 2022 Conference Proceedings*, pages 1–10, 2022.
- [46] Chitwan Saharia, Jonathan Ho, William Chan, Tim Salimans, David J Fleet, and Mohammad Norouzi. Image super-resolution via iterative refinement. *IEEE Transactions on Pattern Analysis and Machine Intelligence*, 2022.
- [47] Tim Salimans and Jonathan Ho. Progressive distillation for fast sampling of diffusion models. *arXiv preprint arXiv:2202.00512*, 2022.
- [48] Tim Salimans, Diederik Kingma, and Max Welling. Markov chain monte carlo and variational inference: Bridging the gap. In *International conference on machine learning*, pages 1218–1226. PMLR, 2015.

- [49] Swami Sankaranarayanan, Anastasios Nikolas Angelopoulos, Stephen Bates, Yaniv Romano, and Phillip Isola. Semantic uncertainty intervals for disentangled latent spaces. In *Advances in Neural Information Processing Systems*, 2022.
- [50] Nicki Skafté, Martin Jørgensen, and Søren Hauberg. Reliable training and estimation of variance networks. *Advances in Neural Information Processing Systems*, 32, 2019.
- [51] Kihyuk Sohn, Honglak Lee, and Xinchen Yan. Learning structured output representation using deep conditional generative models. *Advances in neural information processing systems*, 28, 2015.
- [52] Yang Song and Stefano Ermon. Generative modeling by estimating gradients of the data distribution. *Advances in neural information processing systems*, 32, 2019.
- [53] Yang Song, Jascha Sohl-Dickstein, Diederik P Kingma, Abhishek Kumar, Stefano Ermon, and Ben Poole. Score-based generative modeling through stochastic differential equations. *arXiv preprint arXiv:2011.13456*, 2020.
- [54] Yang Song, Liyue Shen, Lei Xing, and Stefano Ermon. Solving inverse problems in medical imaging with score-based generative models. *arXiv preprint arXiv:2111.08005*, 2021.
- [55] Yang Song, Prafulla Dhariwal, Mark Chen, and Ilya Sutskever. Consistency models. *arXiv preprint arXiv:2303.01469*, 2023.
- [56] Lucas von Chamier, Romain F Laine, Johanna Jukkala, Christoph Spahn, Daniel Krentzel, Elias Nehme, Martina Lerche, Sara Hernández-Pérez, Pieta K Mattila, Eleni Karinou, et al. Democratising deep learning for microscopy with zerocostdl4mic. *Nature communications*, 12 (1):2276, 2021.
- [57] Guotai Wang, Wenqi Li, Michael Aertsen, Jan Deprest, Sébastien Ourselin, and Tom Vercauteren. Aleatoric uncertainty estimation with test-time augmentation for medical image segmentation with convolutional neural networks. *Neurocomputing*, 338:34–45, 2019.
- [58] Yinhuai Wang, Jiwen Yu, and Jian Zhang. Zero-shot image restoration using denoising diffusion null-space model. *The Eleventh International Conference on Learning Representations*, 2023.
- [59] Richard Zhang, Phillip Isola, and Alexei A Efros. Colorful image colorization. In *Computer Vision—ECCV 2016: 14th European Conference, Amsterdam, The Netherlands, October 11–14, 2016, Proceedings, Part III 14*, pages 649–666. Springer, 2016.

Appendices

A Experimental details

Architectures In all experiments, we used a simple U-Net [44, 11] architecture with four down-sampling/upsampling levels. Downsampling was achieved using 2×2 Maxpooling, and upsampling was performed using resize-convolutions [38] with nearest-neighbor interpolation. The input image is first projected to 32 feature channels using two conv layers. Then, at each level, the encoder halves the spatial resolution and doubles the number of channels using two conv layers to result in 32, 64, 128, and 256 channels at levels 1 to 4 with the output of 4 being the encoder’s bottleneck. The final output is given by a 1×1 convolution reducing the number of channels to 1 for gray-scale images and to 3 for RGB images. Throughout the network, we used LeakyReLU activations with a negative slope of 0.1 for non-linearities and instance normalization to z-score feature activations. For training NPPC to wrap around pre-trained mean estimators, we used the same U-Net and only changed the number of output filters at the last layer to be K or $3K$ for gray-scale or RGB images, respectively. The resulting output channels were then reshaped to K independent images constituting w_1, \dots, w_K . While we are aware of more advanced U-Net variants such as [14, 53, 37], these improvements are orthogonal to NPPC. Therefore, in this work, we kept it as simple as possible.

Per-task details In the super-resolution task we upsampled the low-resolution image using nearest neighbor interpolation prior to feeding it to the network. For the posterior mean prediction, we only learned the required residual from the input to produce the prediction. Similarly, for the inpainting task, we only learned the missing part and produced the prediction by summing the input with the masked output to not waste capacity. For all face models, we learned the directions on full images of resolution 256×256 . On the other hand, for the biological image-to-image translation task, we did not use residual learning as the input and output are not similar. In addition, we learned the directions on 64×64 patches cropped from the full 1024×1024 images, as cell information tends to

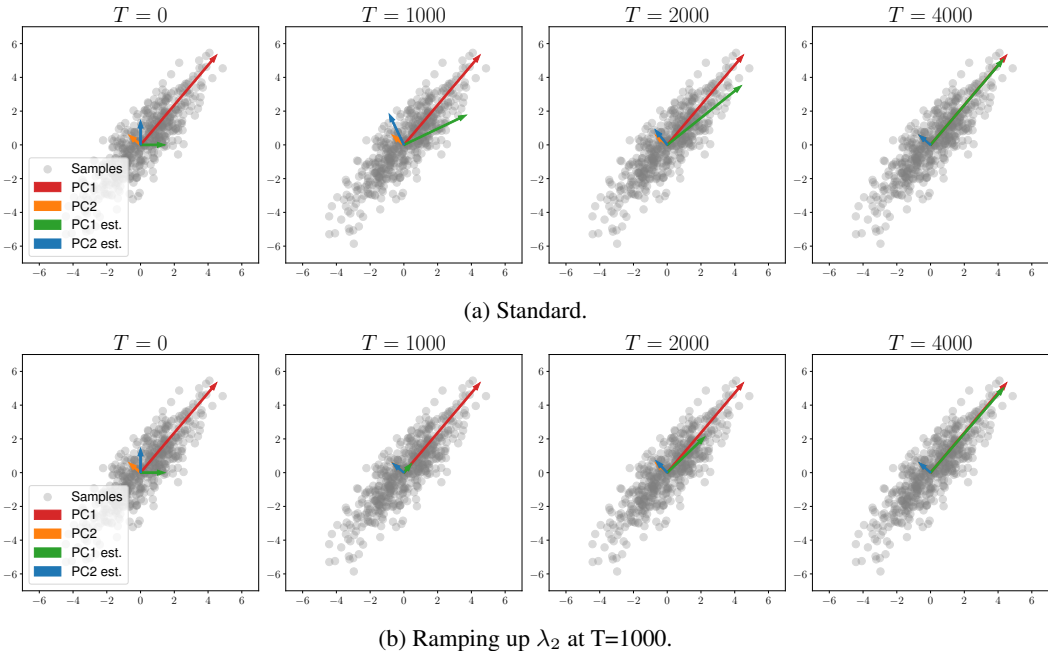


Figure A1: **Scheduling λ_2 for a fixed $\hat{x} = 0$.** In (a) we visualize the optimization steps while estimating the PCs and the variances at the same time, as opposed to ramping up λ_2 after 1000 steps in (b). Notice that at step $T = 1000$, the estimated PCs in (a) (blue and green arrows) are still not aligned with the ground truth PCs compared to (b), due to the optimization of their norms. Eventually, after $T = 4000$ steps both strategies converge to the same solution.

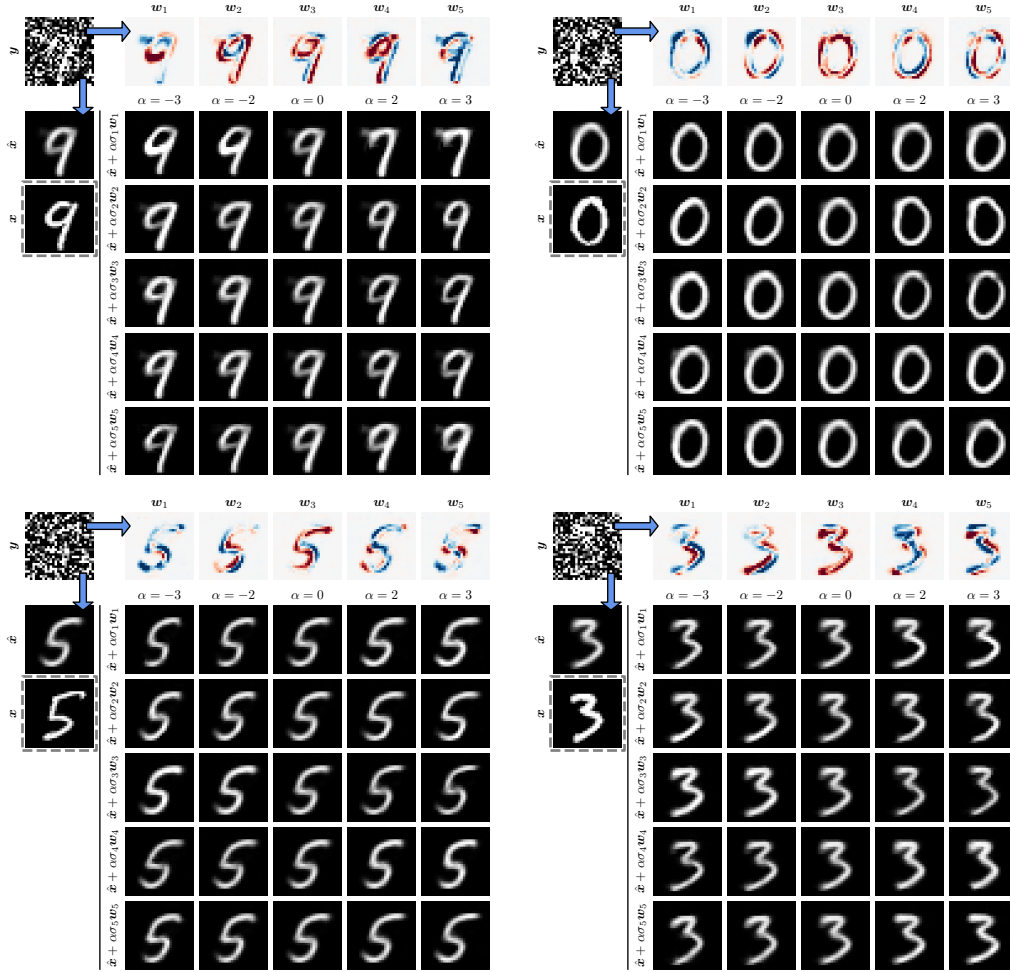


Figure A2: **Joint learning of \hat{x} and w_1, \dots, w_K .** Here we present the results of training a single model to predict both the mean \hat{x} and the PCs w_1, \dots, w_K on the task of denoising handwritten digits. While the resulting model is able to achieve similar results to two separate models (one for estimating the mean and one for estimating the PCs), this necessitated a U-net with double the number of channels compared to the model used in Fig. 4a, leading to an architecture with approximately $4\times$ the number of parameters.

be local. Our architecture is fully convolutional, and hence at test time, we tested on bigger patches of 128×128 as shown in Fig. 6 in the main text, with more examples in Appendix D.

Optimization For all experiments with used the Adam optimizer [21] with an initial learning rate of 0.001, and $\beta_1 = 0.9, \beta_2 = 0.999$. For the CelebA-HQ experiments, the learning rate was dropped by a factor of 10 if the validation loss stagnated for more than 5 epochs, and the minimum learning rate was $5 \cdot 10^{-6}$. For other tasks, we did not use this scheduler, as the results were roughly the same with or without dropping the learning rate. The batch size and the number of epochs were tuned per task according to available GPU memory: batch size of 128 and 300 epochs for MNIST, 16 and 50 for CelebA-HQ, and 64 and 1800 for the biological dataset. When wrapping around a fixed posterior mean predictor, it took about 20 minutes, 5 hours, and 2 hours to train NPPC on MNIST, CelebA-HQ, and the biological data, respectively. In cases where NPPC also predicts the mean jointly with the directions, it took roughly $2\times$ longer (e.g., ≈ 40 minutes for MNIST) due to a more expressive model and the scheduling explained next.

Jointly predicting \hat{x} and scheduling λ_1, λ_2 Training NPPC to predict both the posterior mean \hat{x} and the PCs w_1, \dots, w_K with their variances $\sigma_1^2, \dots, \sigma_k^2$ requires delicate scheduling. The reason

for this instability is that for PCA to work properly the data needs to be centered with zero mean. Hence, during the early iterations when the mean estimate hasn't converged yet, estimating the PCs and the variances along them is challenging. In the extreme case of a trivial mean estimate $\hat{\mathbf{x}} = \mathbf{0}$, the first PC converges to the mean and hence bears little meaning with respect to our purpose. To remedy this, we can ramp up the loss functions sequentially; *i.e.*, initially only \mathcal{L}_μ is on, and after 20 epochs we turn on the PCs and variances loss functions. However, turning both losses \mathcal{L}_w and \mathcal{L}_σ at the same time would lead to a similar conflicting behavior, as in the early iterations the model will try to optimize the variances along random directions. Hence, while we empirically find this to work given enough time for convergence, we opted to ramp up λ_2 after another 20 epochs such that the PCs are almost converged, and only their norm is being optimized. In Fig. A1 we visualize this effect in a 2D toy example of correlated Gaussian samples. Note that predicting both the mean and the directions requires an architecture with enough capacity to handle both tasks (see Fig. A2), especially for severely ill-posed problems. Therefore, for our CelebA-HQ and biological dataset experiments, we focused on a two-step setting where the mean estimate is first learned using a separate U-Net, and afterward, the result is wrapped around with NPPC predicting only the PCs and the variances. We found this strategy to require a significantly lighter model (*e.g.*, 4 \times on MNIST denoising), while also stabilizing training and mitigating the need for scheduling λ_1 and λ_2 .

Loss normalization Learning the PCs and the variances using (4) and (5) is straightforward. Nonetheless, to standardize the loss values across tasks and datasets, we used a slightly modified loss by reweighting the terms for the i^{th} example with the error norm $\|e_i\|$; *i.e.*, for (4) we divided the term $|\mathbf{w}_k(\mathbf{y}_i, \hat{\mathbf{x}}_i; \varphi)^\top e_i|^2$ by $\|e_i\|^2$, and for (5) we divided the inner term by $\|e_i\|^4$. This normalization has two benefits: 1. It standardizes the loss values by the difficulty of the task at hand on a per-sample basis. Meaning, for harder samples the PCs are expected to capture more of the error norm while being allowed an error margin in estimating the variances. 2. This facilitates a constant set of weights $\lambda_1 = 1, \lambda_2 = 1$ across tasks, thus overcoming the need for expensive hyperparameter tuning.

Predicting per-pixel variance For jointly predicting a mean estimate $\hat{\mathbf{x}}$ and a per-pixel variance map $\hat{\sigma}_i^2$ (*e.g.*, in Fig. 1a), we trained a U-Net with two outputs to minimize the loss function

$$\mathcal{L}_{\text{per-pixel}}(\mathcal{D}, \theta) = \sum_{(\mathbf{x}_i, \mathbf{y}_i \in \mathcal{D})} \|\hat{\mathbf{x}}_i(\mathbf{y}_i; \theta) - \mathbf{x}_i\|_2^2 + \|\hat{\sigma}_i^2(\mathbf{y}_i; \theta) - (\hat{\mathbf{x}}_i(\mathbf{y}_i; \theta) - \mathbf{x}_i)^2\|_2^2. \quad (\text{A1})$$

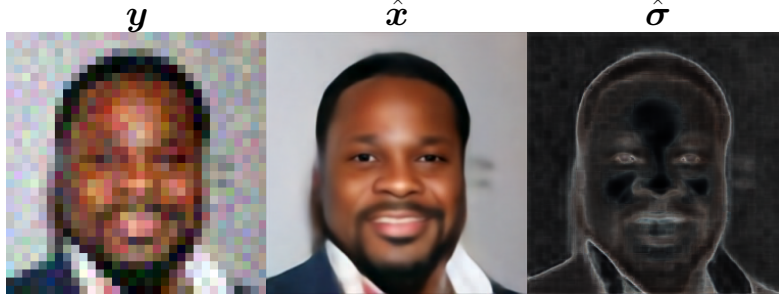
Note that this is slightly different from the standard maximum likelihood approach for predicting $\hat{\sigma}$ (*e.g.*, as in [20]), where the loss is given by

$$\mathcal{L}_{\text{NLL}}(\mathcal{D}, \theta) = \sum_{(\mathbf{x}_i, \mathbf{y}_i \in \mathcal{D})} \frac{\|\hat{\mathbf{x}}_i(\mathbf{y}_i; \theta) - \mathbf{x}_i\|_2^2}{\hat{\sigma}_i^2(\mathbf{y}_i; \theta)} + \log \hat{\sigma}_i^2(\mathbf{y}_i; \theta). \quad (\text{A2})$$

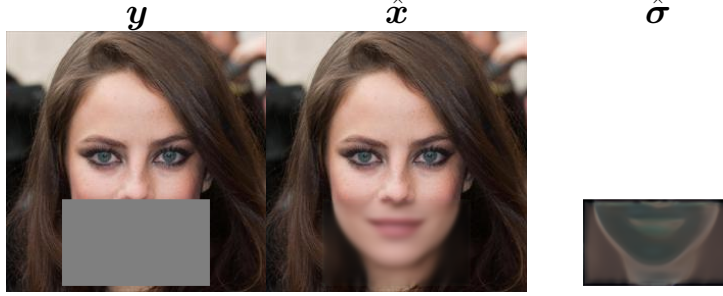
Nonetheless, as previously suggested in numerous works (*e.g.*, [2]), we found the MLE approach not stable and difficult to optimize even when reparameterizing and predicting $\mathbf{s}_i = \log \hat{\sigma}_i^2$. Therefore, in similar spirits to the loss employed to predict the error norm in [2], we optimized (A1) instead. In Fig. A3 we show representative estimated $\hat{\sigma}$ maps on the tasks of 8 \times noisy super-resolution and inpainting from the CelebA-HQ experiments.

B Analytical posterior for Gaussian mixture denoising

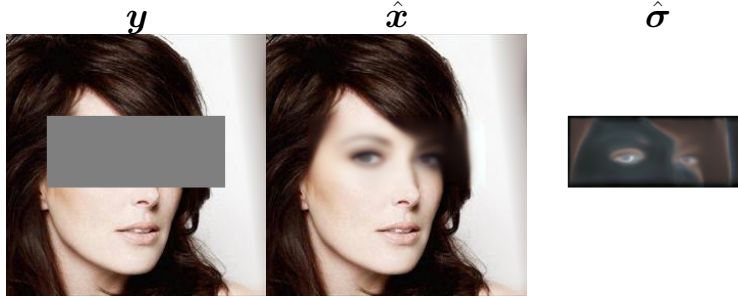
In Figure 3 and Table 1, we compared NPPC to the GT posterior for a Gaussian mixture prior with 2 components. Here we provide the closed-form expressions for the analytically derived posterior and its two first moments for completeness. The denoising task we assumed was $\mathbf{y} = \mathbf{x} + \mathbf{n}$, where \mathbf{x} comes from a mixture of $L = 2$ Gaussians, $p(\mathbf{x}) = \sum_{\ell=1}^L \pi_\ell \mathcal{N}(\mathbf{x}; \boldsymbol{\mu}_\ell, \boldsymbol{\Sigma}_\ell)$, and $\mathbf{n} \sim \mathcal{N}(\cdot; \mathbf{0}, \sigma_\epsilon^2 \mathbf{I})$ is a white Gaussian noise. Let \mathbf{c} be a random variable taking values in $\{1, \dots, L\}$ with probabilities $\{\pi_1, \dots, \pi_L\}$. Then we can write the posterior by invoking the law of total probability conditioned



(a) Noisy $8\times$ super-resolution.



(b) Mouth inpainting.



(c) Eyes inpainting.

Figure A3: **Per-pixel variance maps for CelebA-HQ.** Here we show representative per-pixel standard deviation maps for different tasks on CelebA-HQ. Intuitively, areas with high variance correspond to edges (*e.g.*, (a)), and uncertain shapes/colors (*e.g.*, (b) and (c)). However, as explained earlier, these on their own convey little information regarding the different possibilities.

on the event $\mathbf{c} = \ell$,

$$\begin{aligned}
 p(\mathbf{x}|\mathbf{y}) &= \sum_{\ell=1}^L p_{\mathbf{x}|\mathbf{y},\mathbf{c}}(\mathbf{x}|\mathbf{y},\ell) p_{\mathbf{c}|\mathbf{y}}(\ell|\mathbf{y}) \\
 &= \sum_{\ell=1}^L p_{\mathbf{x}|\mathbf{y},\mathbf{c}}(\mathbf{x}|\mathbf{y},\ell) \frac{p_{\mathbf{y}|\mathbf{c}}(\mathbf{y}|\ell) p_{\mathbf{c}}(\ell)}{p_{\mathbf{y}}(\mathbf{y})} \\
 &= \sum_{\ell=1}^L \mathcal{N}(\mathbf{x}; \tilde{\boldsymbol{\mu}}_{\ell}, \tilde{\boldsymbol{\Sigma}}_{\ell}) \frac{q_{\ell} \pi_{\ell}}{\sum_{\ell'=1}^L q_{\ell'} \pi_{\ell'}}, \tag{A3}
 \end{aligned}$$

where we denoted

$$\begin{aligned}
 q_i &= \mathcal{N}(\mathbf{y}; \boldsymbol{\mu}_i, \boldsymbol{\Sigma}_i + \sigma_{\varepsilon}^2 \mathbf{I}), \\
 \tilde{\boldsymbol{\mu}}_i &= \boldsymbol{\mu}_i + \boldsymbol{\Sigma}_i (\boldsymbol{\Sigma}_i + \sigma_{\varepsilon}^2 \mathbf{I})^{-1} (\mathbf{y} - \boldsymbol{\mu}_i) \\
 \tilde{\boldsymbol{\Sigma}}_i &= \boldsymbol{\Sigma}_i - \boldsymbol{\Sigma}_i (\boldsymbol{\Sigma}_i + \sigma_{\varepsilon}^2 \mathbf{I})^{-1} \boldsymbol{\Sigma}_i. \tag{A4}
 \end{aligned}$$

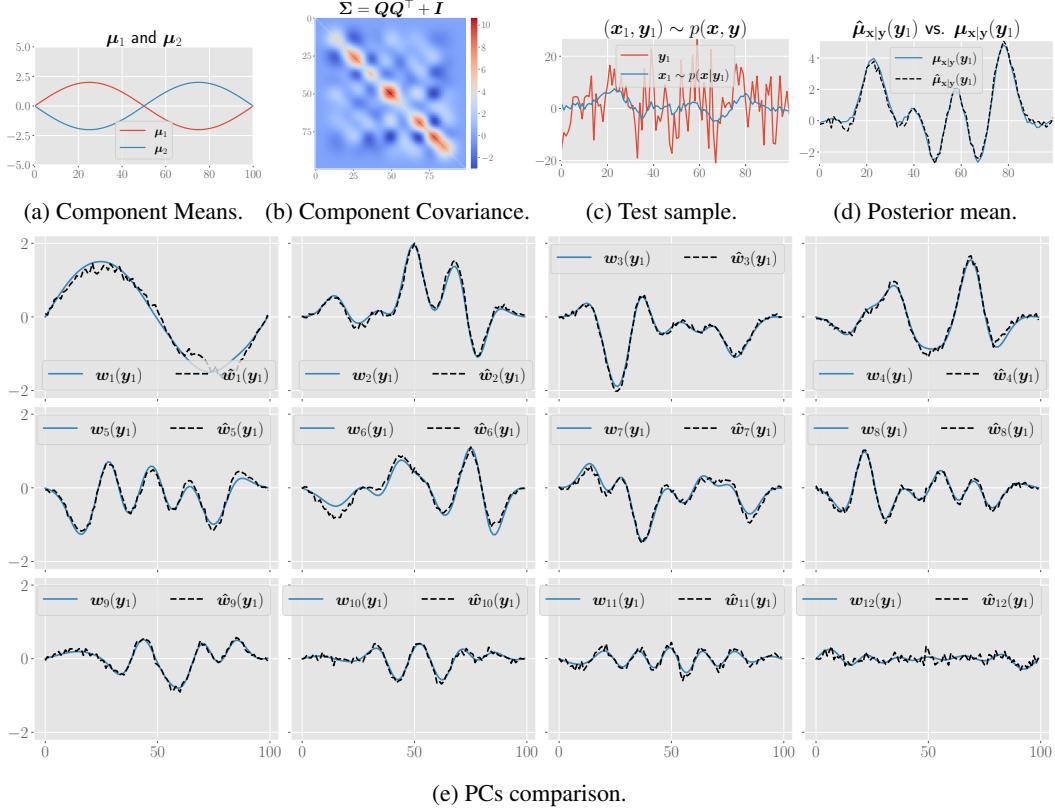


Figure A4: **Denoising samples from a 100-dimensional Gaussian mixture model.** (a) Gaussian mixture means. (b) Covariance matrix of each component. (c) Examined test sample (x_i, y_i) (note that the GT posterior sample x_i is only presented for illustration and is unknown to NPPC). (d) Comparison of the estimated and GT posterior means for the test input y_i in (c). (e) Comparison of the GT (blue) and estimated (dashed black) first 12 PCs scaled by their (respective) GT/estimated σ .

As evident in Fig. 3 and also in Equation (A3), the GT posterior is itself a Gaussian mixture with updated parameters. However, to simplify calculations for the Wasserstein 2-distance comparisons in Table 1, we approximated the GT posterior using a Gaussian with the same first 2 moments, *i.e.*, $p(x|y) \approx \mathcal{N}(x; \mu_{x|y}, \Sigma_{x|y})$, where,

$$\begin{aligned} \mu_{x|y} &= \sum_{\ell=1}^L \tilde{\mu}_\ell \frac{q_\ell \pi_\ell}{\sum_{\ell'=1}^L q_{\ell'} \pi_{\ell'}}, \\ \Sigma_{x|y} &= \sum_{\ell=1}^L \{(\tilde{\mu}_\ell - \mu_{x|y})^2 + \tilde{\Sigma}_\ell\} \frac{q_\ell \pi_\ell}{\sum_{\ell'=1}^L q_{\ell'} \pi_{\ell'}}. \end{aligned} \quad (\text{A5})$$

With this approximation, the Wasserstein 2-distance to the estimated Gaussian constructed by NPPC, $\hat{p}(x|y) = \mathcal{N}(\hat{\mu}_{x|y}, \hat{\Sigma}_{x|y} = \mathbf{W}_* \mathbf{W}_*^\top)$, where \mathbf{W}_* has $\hat{\sigma}_k w_k$ in its k th column, can be efficiently computed using the closed-form expression

$$d_W(p(x|y), \hat{p}(x|y))^2 = \|\mu_{x|y} - \hat{\mu}_{x|y}\|_2^2 + \text{Tr}(\Sigma_{x|y} + \hat{\Sigma}_{x|y} - 2(\Sigma_{x|y}^{1/2} \hat{\Sigma}_{x|y} \Sigma_{x|y}^{1/2})^{1/2}). \quad (\text{A6})$$

Figure A4 visualizes the 100-dimensional Gaussian mixture with $L = 2$ components referred to in Table 1. The component means (A4a) were chosen such that $\mu_1 = -\mu_2$, both with equal weights $\pi_1 = \pi_2 = 0.5$, and the same low-rank covariance matrix $\Sigma_1 = \Sigma_2 = \mathbf{Q}\mathbf{Q}^\top + \mathbf{I}$ with $\text{rank}(\mathbf{Q}) = 12$. Similar to the 2D case, the noise is assumed to be white Gaussian with a per-dimension variance of $\sigma_\varepsilon^2 = 100$. As demonstrated previously in 2D, NPPC is also able to recover the top $K = 12$ PCs and variances accurately in the high-dimensional case.

C Comparison to posterior samplers

In Figure A5, we plot representative comparisons from Table 2 using $K = 5$ PCs as bar plots. The error bars signify a 95% confidence interval constructed using the standard error of the mean. Note that in all tested experiments, NPPC achieved comparable results within the confidence interval of the respective baseline. Moreover, for the task of noisy super-resolution, we observe that only 5 PCs are not enough to capture a significant portion of the error norm (neither by NPPC nor by DDRM [19]). On the other hand, for the task of inpainting, both NPPC and RePaint [28] were able to span a significant portion of the error. To gain a better insight into this phenomenon, in Fig. A6 we plot the fraction of residual error variance against the number of PCs using the posterior samples of DDRM and RePaint. These plots were generated by computing PCA on 100 samples from DDRM and RePaint for each input image. The result suggests that for the task of noisy super-resolution, the error covariance has a wider spread, and the decay rate is significantly slower than for inpainting. For example, using $K = 10$ PCs, the fraction of unexplained variance for super-resolution is ≈ 0.8 compared to ≈ 0.4 for inpainting. This result is not surprising as the optimal number of PCs K is task-dependent and is expected to vary based on the complexity of the posterior. To better exemplify this point, in appendix D.1 we demonstrate the result of NPPC on the task of (face) image colorization.

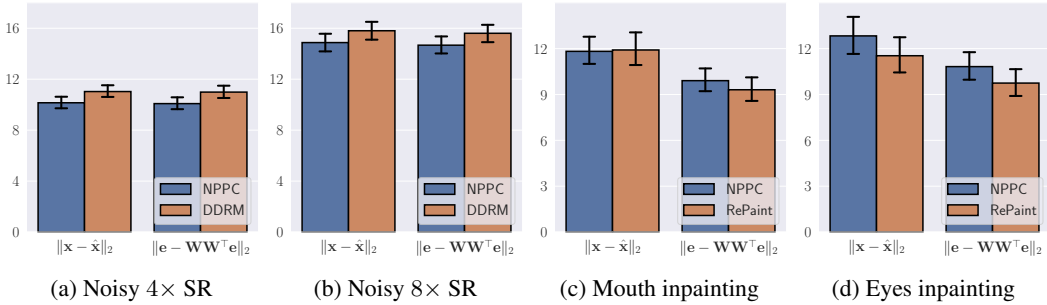


Figure A5: **Comparison to posterior samplers.** Error bars denote a 95% confidence interval constructed using the standard error of the mean. In all tasks (including noiseless super-resolution omitted here for brevity), the performance of NPPC was within a 95% confidence interval around the mean of the respective baseline, sometimes even leading to better results (*e.g.*, (a) and (b)).

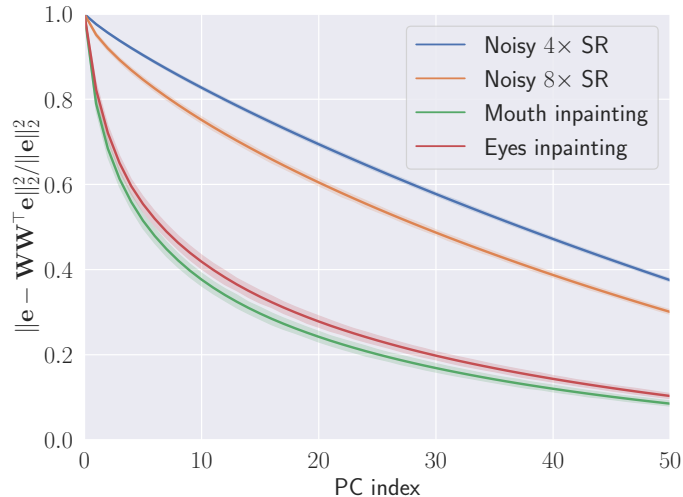


Figure A6: **Fraction of residual error magnitude vs the number of PCs.** Here we visualize the decay in the fraction of unexplained variance (of the error) as more principal components are added. Note that for the task of super-resolution, the decay is significantly slower compared to the task of inpainting. This suggests that multiple PCs roughly capture the same amount of variance, hence explaining the orthogonality of the subspace found by NPPC compared to posterior sampling.

D Additional results

D.1 Image colorization

Inverse problems in imaging vary in their level of difficulty, dictating the complexity of the respective posterior. NPPC is particularly suited for tasks that exhibit strong correlations between output pixels, such that few PCs faithfully span the posterior covariance. One example of such a task is image colorization, where given a grayscale image \mathbf{y} , a model is trained to restore the RGB color image \mathbf{x} . While this task is severely ill-posed, with proper cues and priors encoded in the form of training examples, neural models are able to predict plausible colorizations [59, 24]. Nonetheless, for image regions with multiple possible colorizations, a model trained to minimize the MSE will inevitably regress to the mean producing shades of gray and reflecting dataset bias (e.g., average skin and hair color). Figures A7 and A8 demonstrate the application of NPPC to the problem of face colorization on the CelebA-HQ dataset. First, we trained a model to regress the RGB image \mathbf{x} from the corresponding grayscale input \mathbf{y} . Afterward, we trained NPPC to wrap around the mean estimate $\hat{\mathbf{x}}$, and output the first $K = 5$ PCs. Here, the resulting PCs efficiently capture the majority of the error variance, enabling high-quality reconstructions of the ground truth on test samples, by adding the projected error $\hat{\mathbf{e}}_i = \mathbf{W}_i \mathbf{W}_i^\top \mathbf{e}_i$ to the mean estimate $\hat{\mathbf{x}}_i$. Note that this result uses privileged information (i.e., \mathbf{e}_i) unavailable at test time, and is presented here merely to reinforce our intuition that NPPC is efficient for posteriors with a spectrally-concentrated covariance. In general, using PCs to visualize uncertainty is very appealing as we can efficiently communicate the different possibilities to the user with a few sliders. However, for a large number of PCs K , this strategy becomes impractical and tedious, warranting further research of condensed alternative representations of uncertainty.

D.2 Sequential vs joint PC learning

As explained in Sec. 3.2, we use Stopgrad to recover the solution of sequential training while learning the PCs jointly. Although this is guaranteed in theory, whether the two are equivalent in practice still warrants empirical validation. To realize sequential training without significantly altering the number of parameters used to predict the PCs, we trained multiple models with an increasing number of PCs $K = 1, 2, \dots, 5$, and compared the PCs backward across different models. The results for the task of image colorization on CelebA-HQ confirm that end-to-end training leads to approximately the same PCs as sequential training (see Fig. A9). In addition, the resulting first 5 PCs when training two NNs with 5/10 components were very similar (up to a flipped sign) with an average cosine similarity of 0.9 across the first 3 PCs, and 0.83 overall. For later PCs (e.g. the 4th and 5th) the similarity slightly drops as the error variance along multiple PCs is roughly the same (see Fig. A10), and hence the ordering of the PCs becomes less distinct and prone to optimization errors. These results further validate that NPPC consistently outputs the PCs in the correct order.

D.3 Predicted variance validation

As mentioned in Sec. 3, there exists no ground truth uncertainty in image restoration datasets. This is because each element in the dataset is comprised of a *single* posterior sample \mathbf{x}_i from $p_{\mathbf{x}|\mathbf{y}}(\mathbf{x}|\mathbf{y} = \mathbf{y}_i)$ for each observed image \mathbf{y}_i . This is the reason why beyond toy examples we evaluated the quality of the PCs indirectly using the residual error magnitude $\|\mathbf{e} - \mathbf{W}\mathbf{W}^\top \mathbf{e}\|_2$, which is a function of the subspace spanned by the PCs \mathbf{W} . Similarly, for the k^{th} predicted variance σ_k^2 , we only have the norm of a single projected error $|\mathbf{w}_k^\top \mathbf{e}_i|$ per measurement \mathbf{y}_i , and hence no ground truth variance either. Please note that, unlike per-pixel methods, in our case, we cannot compare the aleatoric uncertainty and the test error directly (e.g. RMSE vs. fraction of pixels above an uncertainty threshold), because our method does not assume pixels are independent (an incorrect assumption in images). Nonetheless, we further verified the predicted variances by comparing the projected test error $\mathbf{w}_k^\top \mathbf{e}_i$ to the predicted variance σ_k^2 for every test point \mathbf{y}_i (see Fig. A10). The results indicate that NPPC estimates the standard deviation with high accuracy across tasks and datasets.

D.4 More examples

Here we provide more results on each of the tasks demonstrated in Section 4.

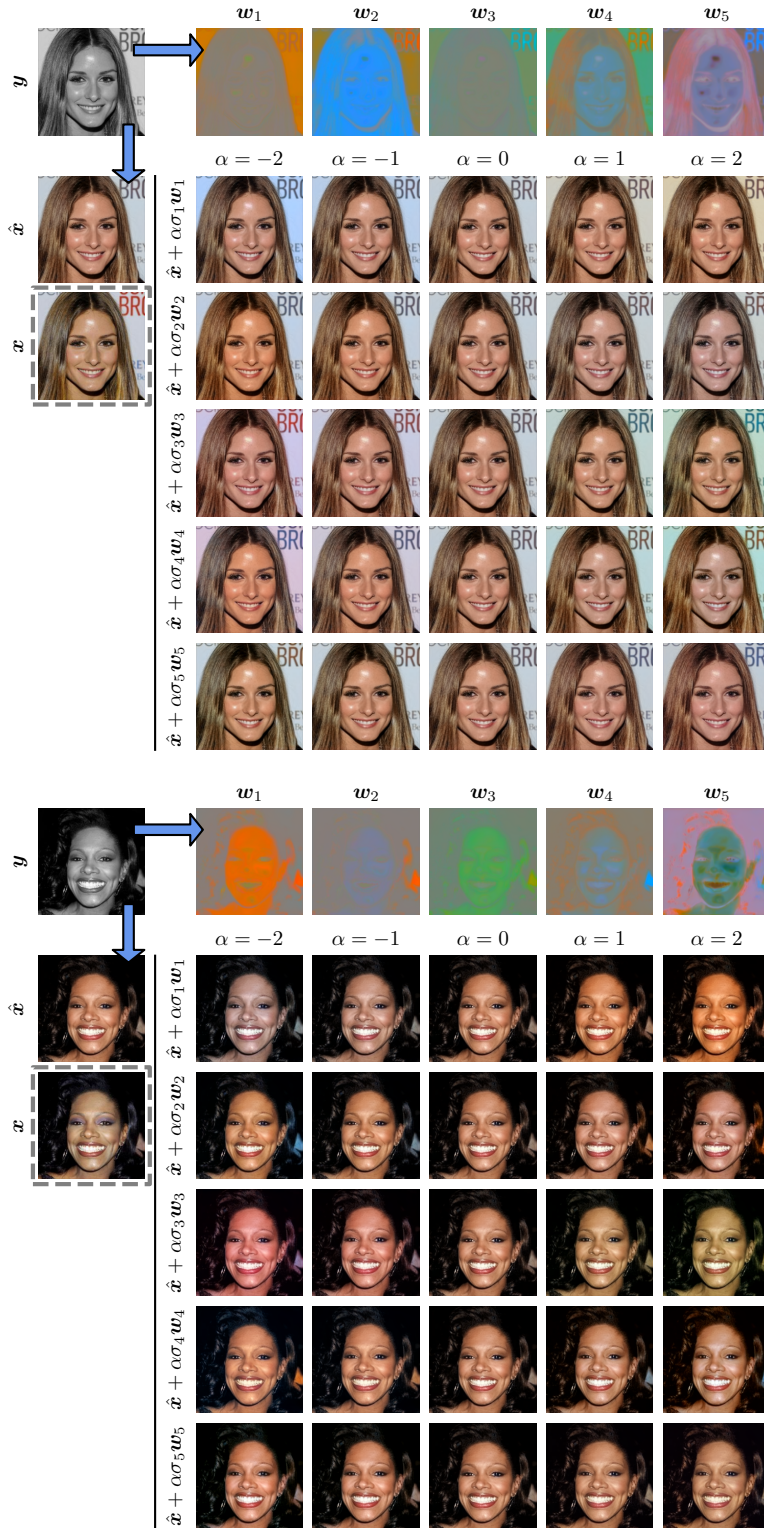


Figure A7: **Face colorization on CelebA-HQ.** Here we showcase the result of NPPC applied to the task of image colorization, *i.e.*, going from a grayscale measurement y to an RGB image x . The resulting PCs span various semantic changes including hair, skin and background colors.

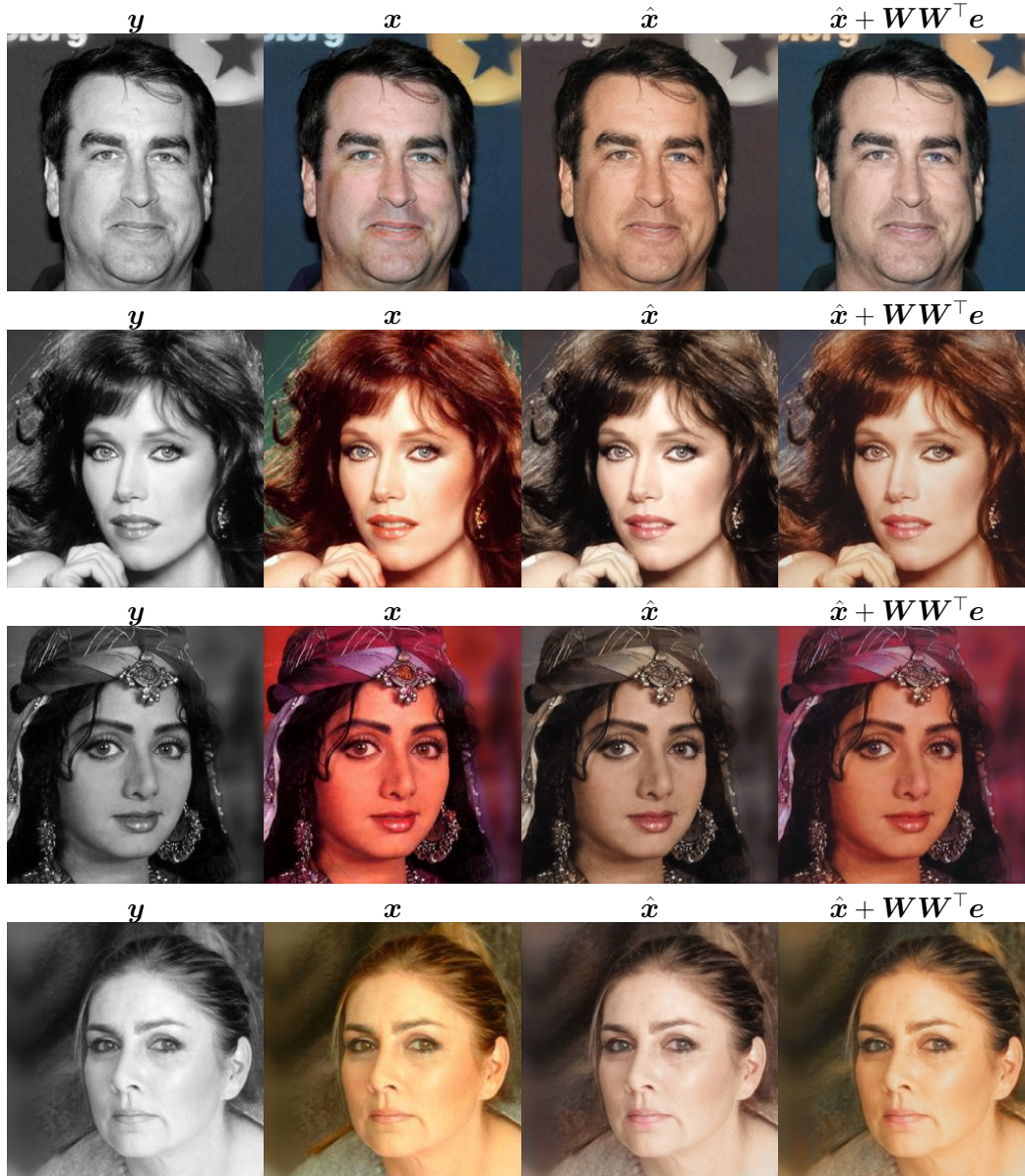


Figure A8: **Reconstructing test samples using 5 PCs.** Here we test the approximation error of the first $K = 5$ PCs found by NPPC by reconstructing the ground truth error $e_i = \hat{x}_i - x_i$ of test samples. The reconstructed error $\hat{e}_i = W_i W_i^\top e_i$ is added to the mean estimate \hat{x}_i to approximate the ground truth RGB image x_i . Note that at test time we do not have access to e_i , therefore this result is only a sanity check to verify our PCs.

Handwritten digits Figure A11 demonstrates more denoising examples for handwritten digits. At severe noise levels of $\sigma_\varepsilon = 1.0$, the mean reconstruction is often ambiguous with regards to digit identity (e.g., a “7” can become a “9” as in the upper left panel). Similarly, for extreme inpainting of 70% of the pixels in Fig. A12, a “5” can become a “3” (top right), a “4” can become a “1” (bottom left), etc.

Faces Figures A13 shows additional examples for the task of noisy $8\times$ super-resolution. The resulting PCs capture different semantic properties such as eye/mouth shape, eyebrows position, and chin/jawline placement. Figures A14 and A15 show additional results for inpainting of the eyes and the mouth, respectively. The corresponding PCs manipulate the content in the missing pixels such

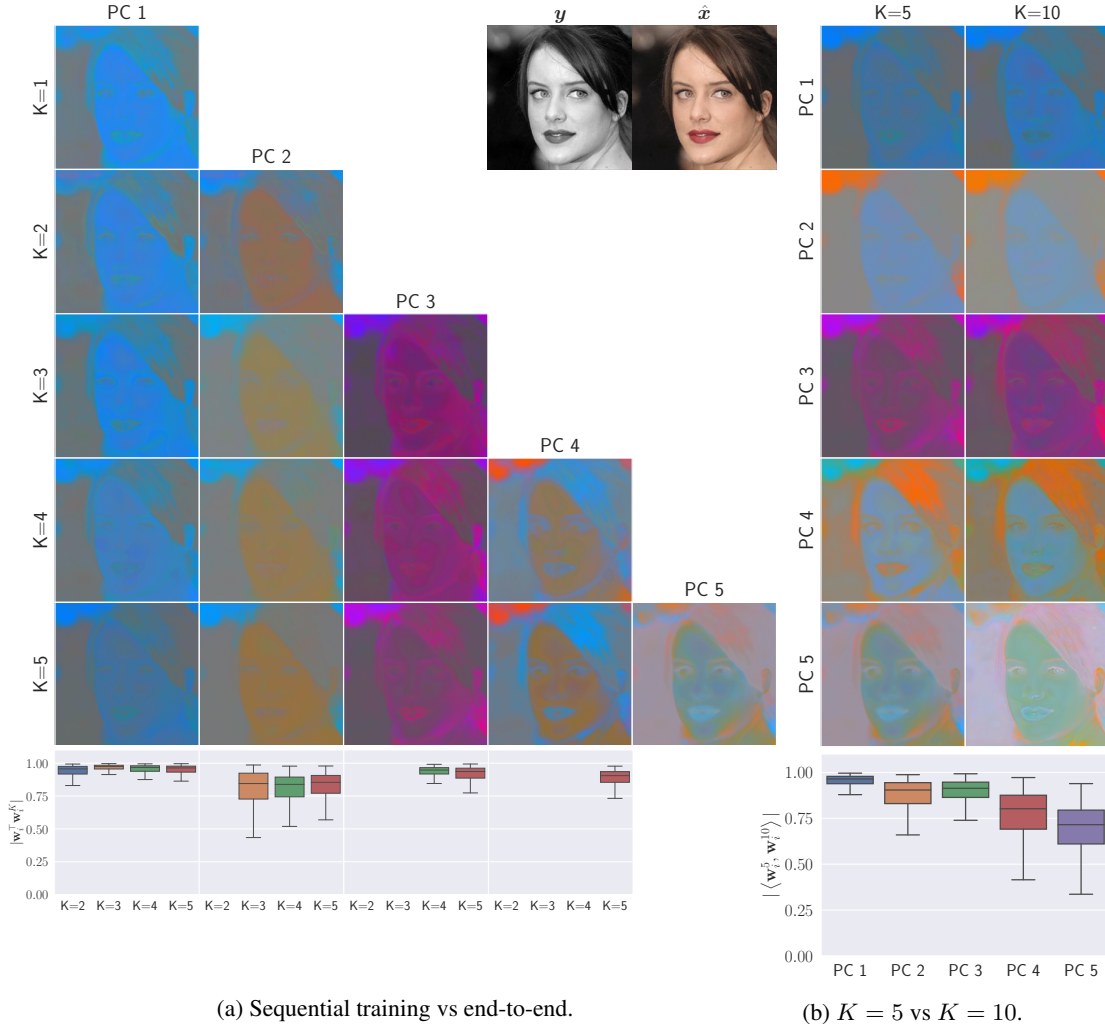


Figure A9: PC consistency as a function of K in image colorization. (a) Sequential and end-to-end PC training are compared using 5 models outputting an increasing number of PCs $K = 1, \dots, 5$. Each row presents K PCs predicted by a model with K outputs applied to the inputs at the top right. The PCs are backward consistent as judged by their absolute cosine similarity over the entire test set (see boxplots at the bottom). (b) The results were similar when comparing the first 5 PCs of two models with $K = 5/10$ outputs, with the last 2 PCs being slightly less consistent due to the remaining PCs having roughly the same variance.

that the eyes (Fig. A14) are more open/closed, the eyebrows are thicker/thinner etc. Similarly, for mouth inpainting (Fig. A15), the mouth could be open/closed, the jaw could be lower/higher, and the neck area is manipulated to be wider/thinner, etc.

Biological image-to-image translation Figures A16 and A17 show additional results on the biological image-to-image translation task. Note that the first PC is essentially a bias component, suggesting that the absolute intensity of the nuclear stains is uncertain and cannot be inferred accurately using the measurement y . The remaining PCs capture more semantic content by highlighting uncertain cell shapes *e.g.*, in the case of dividing (small ellipsoidal) cells and navigating the existence/disappearance of ambiguous cells.

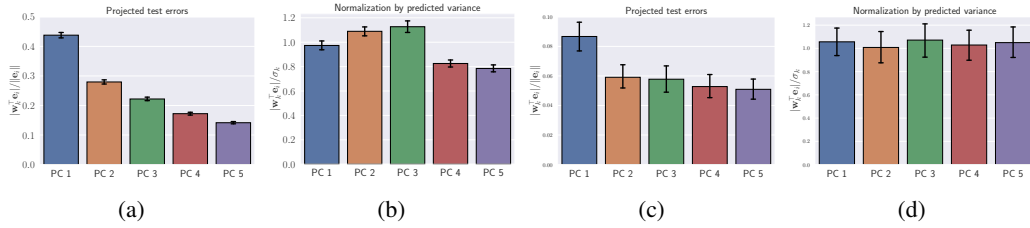


Figure A10: Predicted variance validation. The PC ordering/predicted variances are validated using the projected test errors $|\mathbf{w}_k^\top \mathbf{e}_i| / \|\mathbf{e}_i\|$, and their normalization by the predicted standard deviation $|\mathbf{w}_k^\top \mathbf{e}_i| / \sigma_k$, both for image colorization on CelebA-HQ (a)-(b) and for image denoising on MNIST (c)-(d). As can be seen in (a) and (c) the PCs are correctly ordered from 1 to 5. Furthermore, (b) and (d) show that the predicted variances are accurate with an average standard deviation of 0.96 for CelebA-HQ and 0.99 for MNIST, where 1 is the ground truth.

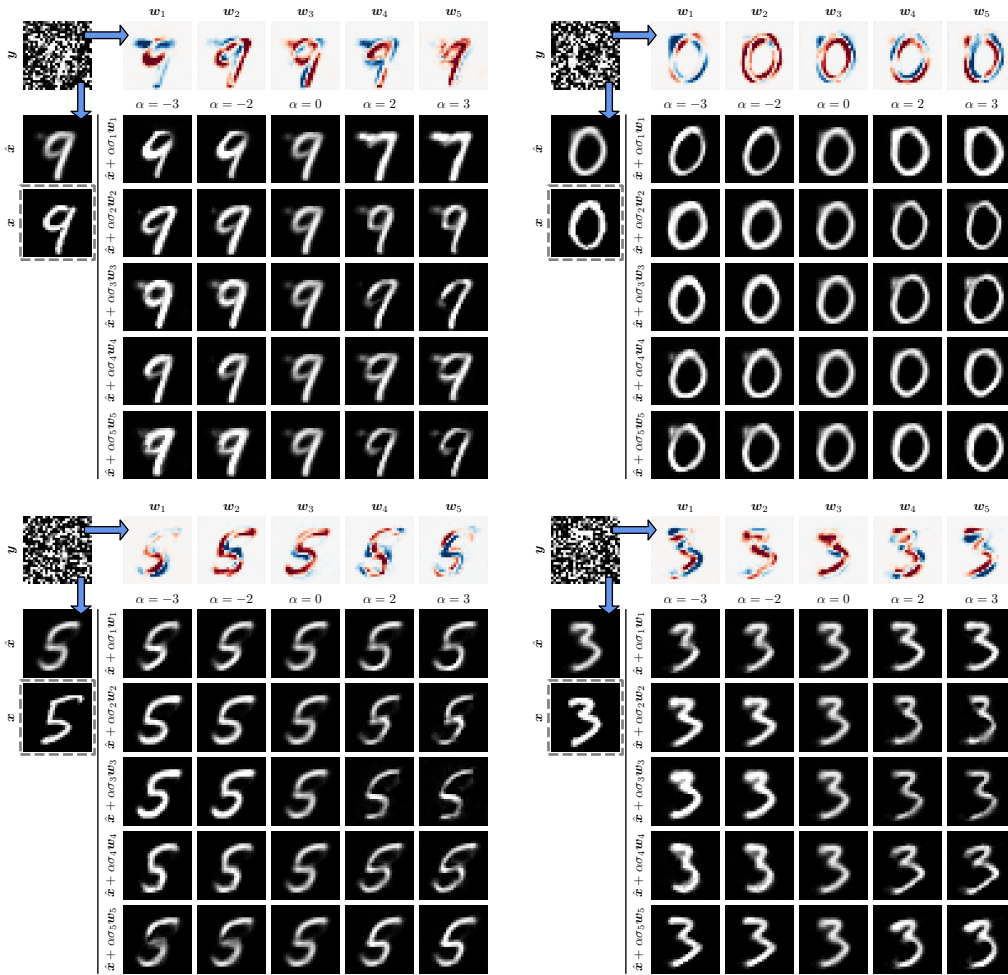


Figure A11: MNIST denoising.

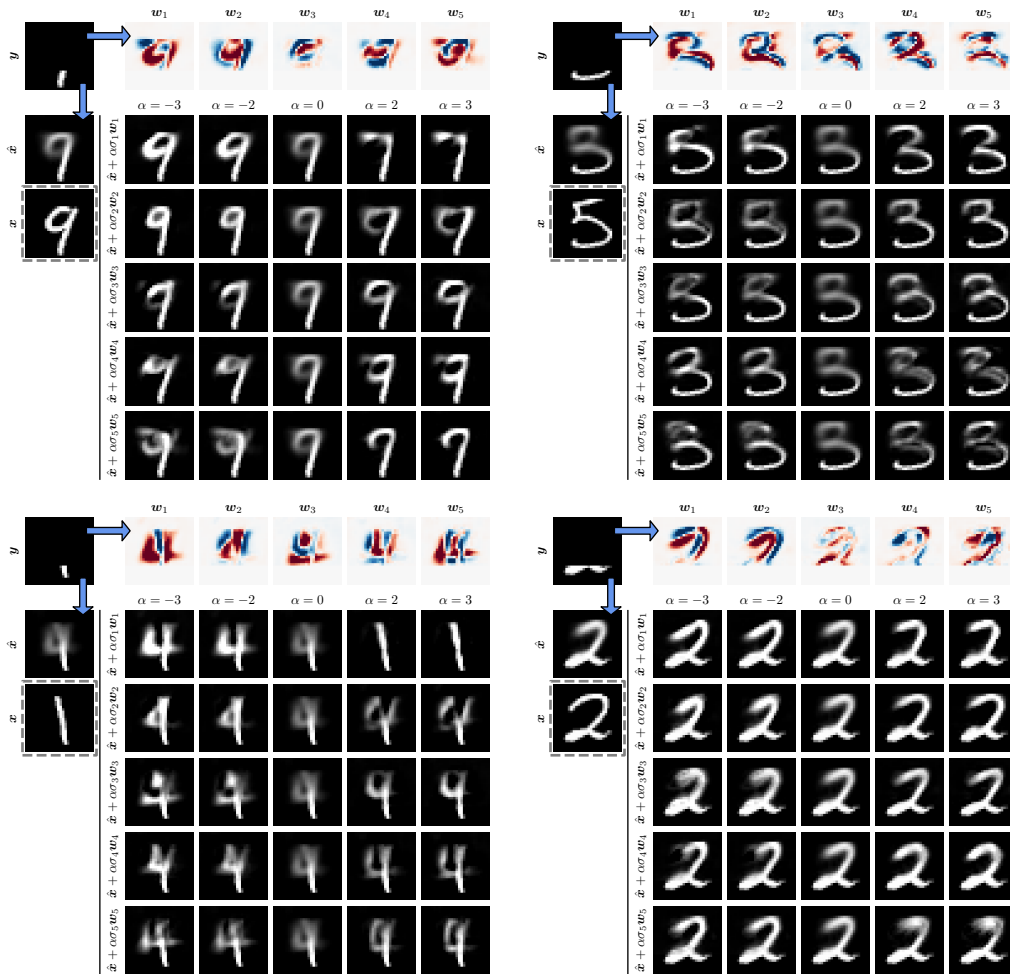


Figure A12: MNIST inpainting.

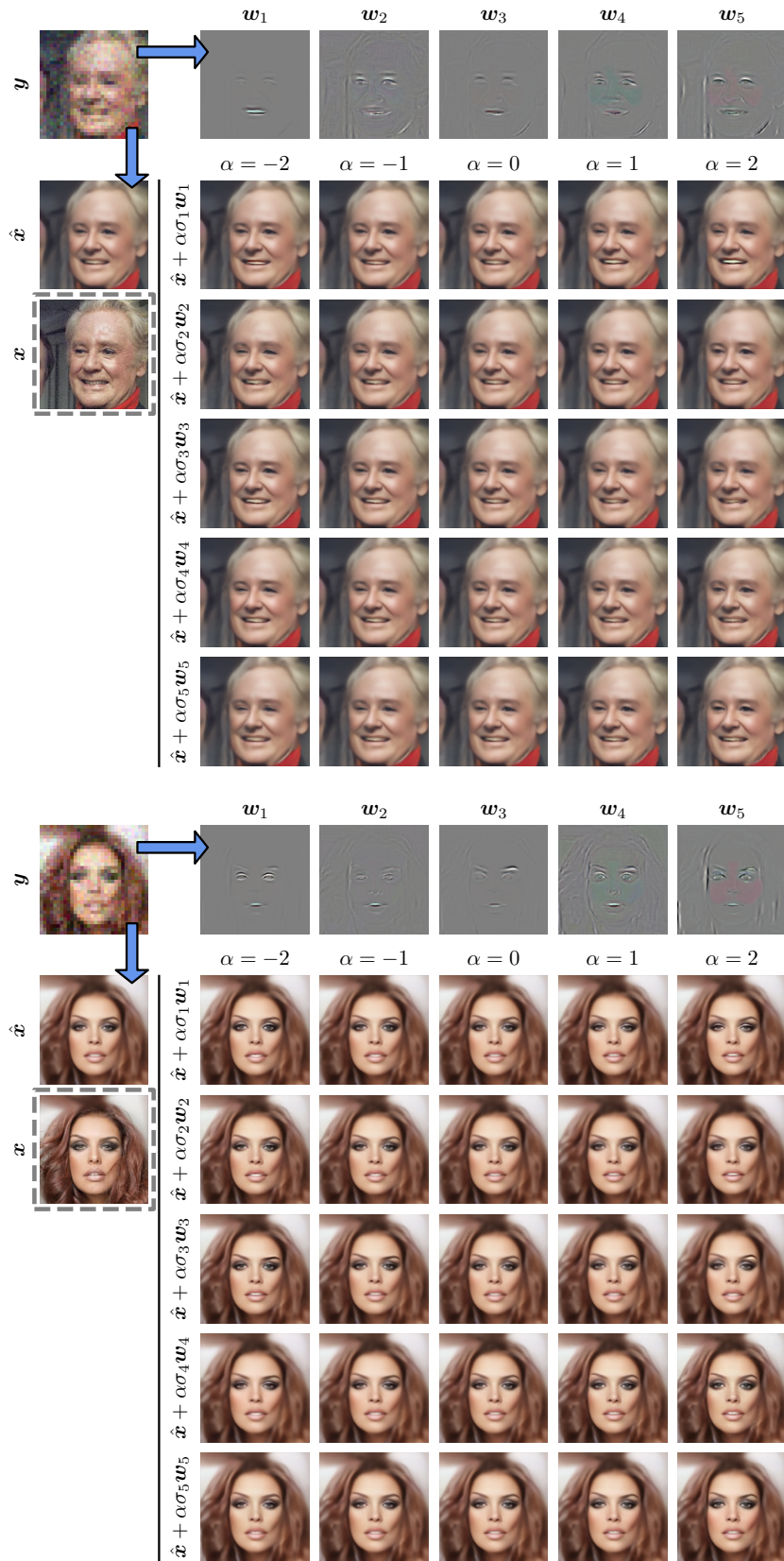


Figure A13: CelebA-HQ noisy 8x super-resolution.

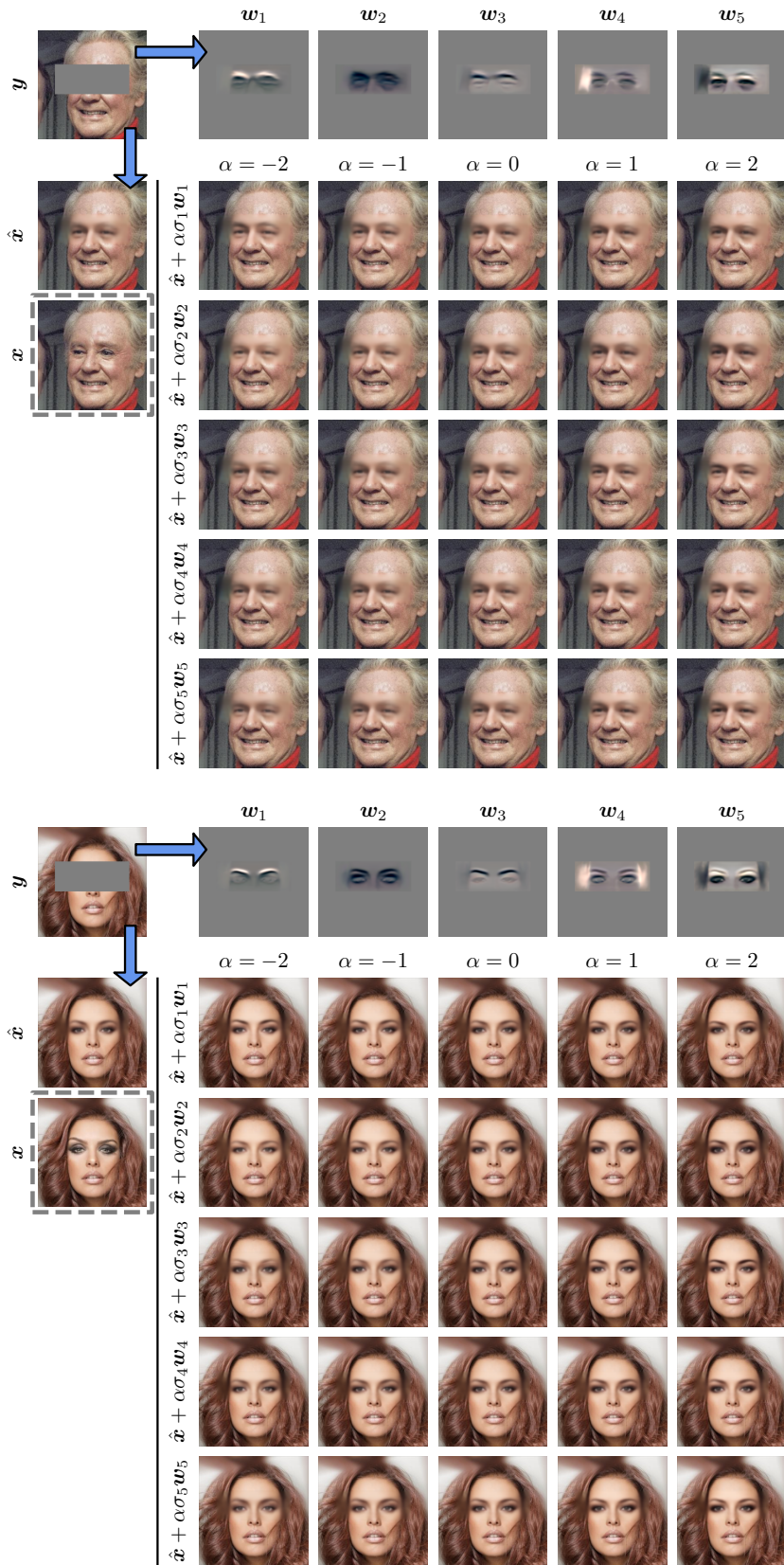


Figure A14: CelebA-HQ eyes inpainting.

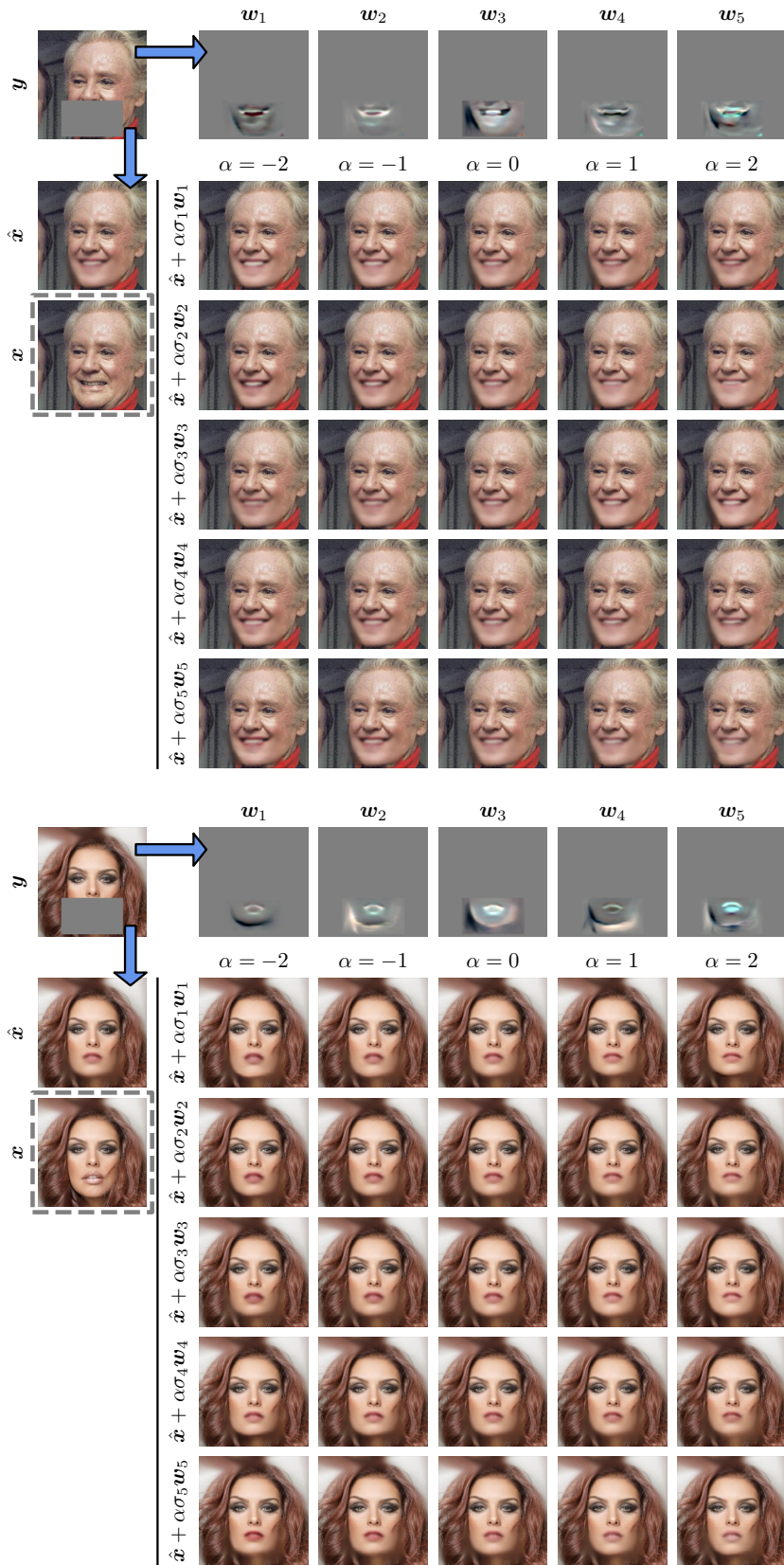


Figure A15: CelebA-HQ mouth inpainting.

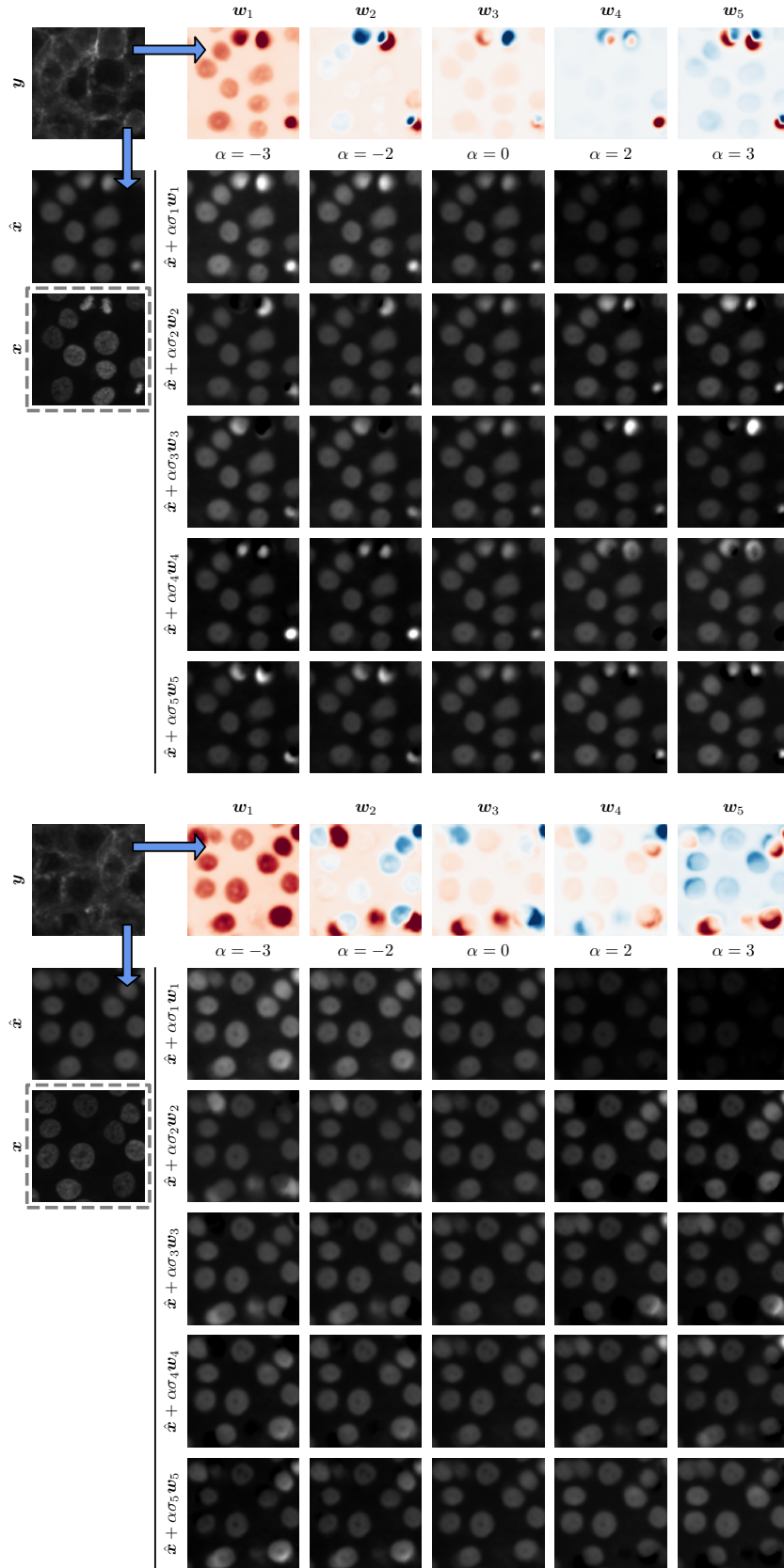


Figure A16: Biological image-to-image translation results.

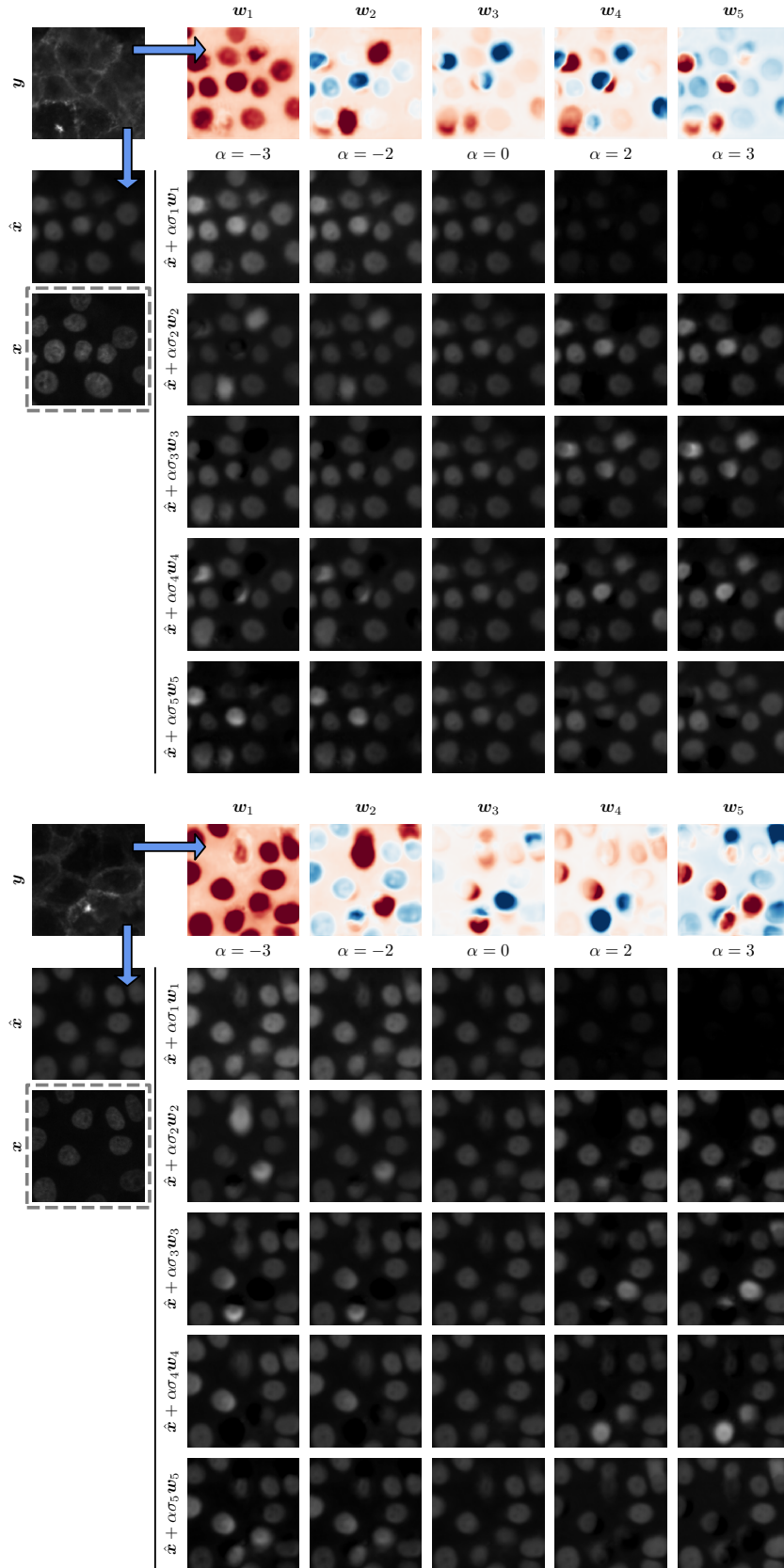


Figure A17: More biological image-to-image translation results.